

Simulation of Dynamic Interface Fracture using Spectral Boundary Integral Method

Thesis by

Ajay Bangalore Harish

In Partial Fulfillment of the Requirements

for the Degree of

Aeronautical Engineer



California Institute of Technology

Pasadena, California

2009

(Submitted 2009-05-15)

Acknowledgements

I consider myself exceptionally fortunate to have had the opportunity to work as a Masters student at Caltech, working with a number of great scientists and wonderful people. The time has finally come to say thanks to them.

Firstly I express my sincere gratitude to my advisor Prof. Nadia Lapusta for all the guidance, inspiration and support. Nadia introduced me to the field of dynamic fracture mechanics and had remarkable patience to spend hours going through research and was always willing to help me see connections between seemingly unrelated results and make everything fit together. This thesis would not have been possible without her critical contributions and insights.

I would also like to thank Prof. Guruswami Ravichandran and Prof. Chiara Daraio for graciously agreeing to be on my thesis committee, reviewing my thesis and providing crucial criticisms and suggestions. Prof. Ravichandran has given me constant support throughout my stay at Caltech. I would also like to thank Prof. Ares Rosakis for the critical insights into the problem.

I would also like to extend my sincere appreciation to my group members - Dr. Yi Liu, Dr. Xiao Lu, Dr. Yoshihiro Kaneko, Ahmed Elbanna and Ting Chen for all the help and support in the last year of stay at Caltech. I specially thank Dr. Yi Liu for providing his 3D code for dynamic shear ruptures on bimaterial interfaces that served as a starting point for the code developed in my work. I am also grateful to Dr. Xiao Lu for discussing with me his experiments and providing his experimental

data for comparison with my modeling. I also thank Maria for all the help extended.

I also like to thank Dr. Harsha Bhat and Mike Mello for all the help and constant advice and suggestions throughout my stay at Caltech. I would also like to extend my appreciation to all my office mates - Bharat Prasad, Phanish Suryanarayana, Daniel Hurtado for all the help. I would also like to thank my colleagues for all the studying we did in the SFL library - Prakhar Mehrotra, Sandeep Kumar Lahiri, Nicholas Boecler, Michio Inoue, Kawai Kwok, Inki Choi, Devvrath Khatri, Celia Reina Roma, Vahe Gabuchian, Jon Mihaly. I also thank my co-TA's Farshid Roumi and Timothy Kwa was making the teaching experience of ME-35 a memorable one. I also thank all my other friends at Caltech who made my stay academically and socially stimulating and to name some - Sujit Nair, Rajani Kurup, Navneet T Narayan, Manav Malhotra, Deb Ray. I whole-heartedly thank everyone who has been of help knowingly and unknowingly.

Last but never the least I whole-heartedly thank my parents for standing by me, believing in me and supporting all my decisions unconditionally through the hard times, without which this would have been impossible.

Abstract

Simulation of three-dimensional dynamic fracture events constitutes one of the most challenging topics in the field of computational mechanics. Spontaneous dynamic fracture along the interface of two elastic solids is of great importance and interest to a number of disciplines in engineering and science. Applications include dynamic fractures in aircraft structures, earthquakes, thermal shocks in nuclear containment vessels and delamination in layered composite materials.

This thesis presents numerical modeling of laboratory experiments on dynamic shear rupture, giving an insight into the experimental nucleation conditions. We describe a methodology of dynamic rupture simulation using spectral boundary integral method, including the theoretical background, numerical implementation and cohesive zone models relevant to the dynamic fracture problem. The developed numerical implementation is validated using the simulation of Lamb's problem of step loading on an elastic half space and mode I crack propagation along a bonded interface. Then the numerical model and its comparison with experimental measurements is used to investigate the initiation procedure of the dynamic rupture experiments. The inferred parameters of the initiation procedure can be used in future studies to model the experimental results on supershear transition and rupture models.

Contents

Acknowledgements	i
Abstract	iii
Contents	v
List of Figures	x
List of Tables	x
1 Introduction	1
1.1 Goal and outline	1
1.2 Description of experiments that motivate our modeling	3
1.2.1 Configuration of the experiment	4
1.2.2 Rupture nucleation mechanism	5
1.3 Relevant experimental observations	7
2 Spectral Boundary Integral Method And Its Numerical Implemen- tation	9
2.1 Introduction to dynamic fracture simulations	9
2.2 Theoretical formulation of the spectral boundary integral method	11
2.3 Numerical implementation of the spectral scheme	18
2.4 Theoretical formulation of cohesive zone laws	22
2.4.1 Ortiz-Camacho Model	23
2.4.2 Reversible rate-independent cohesive model	24

3	Validation of the developed numerical approach	26
3.1	Study of Lamb's problem on an elastic half-space	26
3.1.1	Theoretical formulation of Lamb's problem	26
3.1.2	Numerical investigation of Lamb's problem	28
3.2	Propagating mode-I crack in a plate	31
3.2.1	Critical crack length	31
3.2.2	Cohesive zone length	34
3.2.3	Numerical resolution	35
3.2.4	Numerical simulation of propagating mode I crack in rocks . .	36
4	Simulations of nucleation procedure in laboratory earthquake exper-	
	iments	41
4.1	Comparison of numerically computed and experimentally measured interface-parallel displacements	42
4.1.1	Effect of the explosion pressure	43
4.1.2	Effect of the cohesive zone models	49
4.1.3	Effect of loading duration	51
4.1.4	Effect of plasma spreading speed (C_{pla})	54
4.2	Mode I crack propagation due to the nucleation procedure	56
4.3	Conclusions	58
4.4	Future work	64
	References	71

List of Figures

1.1	Experimental Setup. Adapted from Lu (2009)	4
1.2	Schematic diagram of the exploding wire system coupled with a photoelastic fault model. Adapted from Xia (2005)	6
1.3	Comparison of the experimentally measured interface-parallel displacement for 0-degree and 90-degree points. Adapted from Lu (2009)	8
1.4	Comparison of the experimentally measured interface-parallel velocity for 0-degree and 90-degree points. Adapted from Lu (2009)	8
2.1	Problem Geometry	11
2.2	Convolution kernels in displacement formulation for a Poisson ratio $\nu = 0.35$	18
2.3	Convolution kernels in velocity formulation for a Poisson ratio $\nu = 0.35$	19
2.4	Tensile cohesive relation - Ortiz-Camacho cohesive relation	24
2.5	Reversible rate-independent cohesive model	25
3.1	Evolution of displacement normal to the traction-free surface at a point located at a distance L from the point of application of load. Dotted lines denote the arrival times of dilatational, shear and Rayleigh waves.	29
3.2	Displacement field on the surface of the half space after 200 time steps, showing the concentric waves expanding from the point of application of point load	30
3.3	A funnel crack in a plate subjected to external loads.	32
3.4	Propagation of mode I crack across the domain with time (0, 0.10, 0.20, 0.30 μs)	38

3.5	Propagation of mode I crack across the domain with time (0.35, 0.40, 0.45, 0.50 μ s)	38
3.6	Propagation of mode I crack across the domain with time (1, 2, 3, 4 μ s)	39
3.7	Propagation of mode I crack across the domain with time (5, 6, 7, 8 μ s)	39
4.1	The pressure profile used to model the explosion. P_{max} is the maximum pressure. t_1 , t_2 and t_3 are the time parameters of the loading profile. . .	44
4.2	Comparison of interface-parallel displacement at a distance of 10 mm from the point of explosion for loading profile 2 and parameters $P_{max} = 1,2,3,4,10$ GPa and $t_1 = 0\mu$, $t_2 = t_3 = 5\mu$ s. The numerical simulation being governed by Ortiz-Camacho cohesive zone model.	45
4.3	Comparison of interface-parallel displacement at a distance of 10 mm from the point of explosion for loading profile 2 and parameters $P_{max} = 1,2,3,4,10$ GPa and $t_1 = 0\mu$, $t_2 = t_3 = 5\mu$ s. The numerical simulation being governed by reversible rate-independent cohesive zone model. . .	46
4.4	Comparison of interface-parallel displacement at a distance of 10 mm from the point of explosion for loading profile 2 and parameters $P_{max} = 1,2,3,4,10$ GPa and $t_1 = 0\mu$, $t_2 = 4\mu$ s, $t_3 = 5\mu$ s. The numerical simulation being governed by Ortiz-Camacho cohesive zone model. . .	47
4.5	Comparison of interface-parallel displacement at a distance of 10 mm from the point of explosion for loading profile 2 and parameters $P_{max} = 1,2,3,4,10$ GPa and $t_1 = 0\mu$, $t_2 = 4\mu$ s, $t_3 = 5\mu$ s. The numerical simulation being governed by reversible rate-independent cohesive zone model.	48
4.6	Comparison of interface-parallel displacement, for numerical simulations governed by Ortiz-Camacho cohesive zone model and reversible rate-independent cohesive zone model, at a distance of 10 mm from the point of explosion for loading profile 1 with parameters $P_{max} = 10$ GPa and $t_1 = 0\mu$, $t_2 = t_3 = 5\mu$ s.	49

4.7	Comparison of interface-parallel displacement, for numerical simulations governed by Ortiz-Camacho cohesive zone model and reversible rate-independent cohesive zone model, at a distance of 10 mm from the point of explosion for loading profile 2 with parameters $P_{\max} = 10$ GPa and $t_1 = 0\mu$, $t_2 = 4\mu s$, $t_3 = 5\mu s$	50
4.8	Comparison of interface-parallel displacement, for numerical simulations governed by Ortiz-Camacho cohesive zone model, at a distance of 10 mm from the point of explosion for loading profile 1 with parameters $P_{\max} = 10$ GPa and $t_1 = 1,2,3,4 \mu$, $t_2 - t_1 = 3 \mu s$ and $t_3 - t_2 = 1 \mu s$	52
4.9	Comparison of interface-parallel displacement, for numerical simulations governed by Ortiz-Camacho cohesive zone model, at a distance of 10 mm from the point of explosion for loading profile 1 with parameters $P_{\max} = 10$ GPa and $t_1 = 2 \mu$, $t_2 - t_1 = 3,4,5 \mu s$ and $t_3 - t_2 = 1 \mu s$	53
4.10	The best match between the simulations and the experimental results. The parameters used are $P_{\max} = 10$ GPa, $t_1 = 2 \mu s$, $t_2 - t_1 = 4 \mu s$, $t_3 - t_2 = 1 \mu s$ and $C_{pla} =$ crack tip speed.	54
4.11	Comparison of interface-parallel displacement, for numerical simulations governed by Ortiz-Camacho cohesive zone model, at a distance of 10 mm from the point of explosion for loading profile plasma speeds of $C_{pla} = 250$ m/s, 340 m/s, 500 m/s. The loading parameters are $P_{\max} = 10$ GPa, $t_1 = 1 \mu$, $t_2 = 4 \mu s$, $t_3 = 5 \mu s$	55
4.12	Opening velocity in the nucleation region (at $t = 0, 25, 50, 75$ ns)	56
4.13	Opening velocity in the nucleation region (at $t = 0.1, 0.2, 0.3, 0.4 \mu s$) . .	57
4.14	Opening velocity in the nucleation region (at $t = 0.5, 0.6, 0.7, 0.8 \mu s$) . .	57
4.15	Opening displacement in the nucleation region (at $t = 0, 25, 50, 75$ ns) .	58
4.16	Opening displacement in the nucleation region (at $t = 0.1, 0.2, 0.3, 0.4 \mu s$)	59
4.17	Opening displacement in the nucleation region (at $t = 0.5, 0.6, 0.7, 0.8 \mu s$)	60
4.18	Opening velocity in the domain (at $t = 1, 2, 3, 4 \mu s$)	61
4.19	Opening velocity in the domain (at $t = 5, 6, 7, 8 \mu s$)	61
4.20	Opening velocity in the domain (at $t = 9, 10, 11, 12 \mu s$)	62

4.21	Opening displacement in the domain (at $t = 1, 2, 3, 4 \mu\text{s}$)	62
4.22	Opening displacement in the domain (at $t = 5, 6, 7, 8 \mu\text{s}$)	63
4.23	Opening displacement in the domain (at $t = 9, 10, 11, 12 \mu\text{s}$)	63

List of Tables

1.1	Summary of mechanical properties of Homalite-100	5
3.1	Numerical resolution of critical crack length and cohesive zone length for various levels of prestress	36
4.1	Summary of loading parameters used to study the effect of P_{\max}	44

Chapter 1

Introduction

1.1 Goal and outline

Modeling and simulation of dynamic fracture events is an important topic of computational and experimental mechanics. Dynamic fracture is especially important in the field of geophysics, in the simulation of earthquakes. Earthquakes are destructive processes that occur as dynamical ruptures along the pre-existing faults (interfaces) in the Earth's crust. The practical goal of earthquake seismology is to prevent or reduce human and material losses by estimating the earthquake hazard at a given site or by forecasting the occurrence of the next strong event. Detailed seismic inversions have significantly improved our understanding of earthquake rupture processes. But yet the progress has been less due to the fact that Earth is a complex system.

This highlights the necessity for controlled laboratory experiments and extensive numerical modeling of the dynamic rupture process along an interface. One example of such experiments is work of Xia *et al.* (2004) which demonstrated, for the first time, the transition of shear mode II ruptures from sub-Rayleigh to supershear speeds. Further experiments were conducted by Lu *et al.* (2009), Lu (2009) to study the supershear transition and rupture modes. An approximate numerical modeling of the experiment was developed by Lu *et al.* (2009).

This thesis presents numerical modeling of laboratory dynamic rupture experiments,

giving an insight into the experimental nucleation conditions. In chapter 1, we present a review of the experimental techniques used in the laboratory dynamic rupture experiments and relevant experimental observations. In chapter 2, we discuss the methodology of dynamic rupture simulation using spectral-boundary integral method - both theoretical formulation and numerical implementation. Also in the same chapter we discuss the various cohesive laws relevant to the dynamic fracture problem. In chapter 3, the numerical model developed in chapter 2 is validated using a half-space simulation of Lamb's problem. In chapter 4, the numerical model is used for investigating the initiation procedure in dynamic rupture experiments (Xia (2005), Lu (2009)). Using conceptual loading profiles, we determine the propagation of an opening mode due to the explosive initiation procedure and compare our simulations with experimental results of Lu (2009). In chapter 5, we discuss the conclusions of the work and directions for future work.

Understanding whether supershear transition observed in rupture experiments (Xia *et al.* (2004), Lu *et al.* (2009)) is affected by nucleation procedure is the ultimate goal of the present work. Supershear transition has been a topic of research dating back to early 70's (Burridge (1973); Andrews (1976); Das & Aki (1977); Burridge *et al.* (1979); Freund (1979); Day (1982); Broberg (1989); Needleman & Rosakis (1999); Abraham & Gao (2000); Madariaga & Olsen (2000); Gao *et al.* (2001); Geubelle & Kubair (2001); Dunham & Archuleta (2005); Festa & Vilotte (2006); Rosakis *et al.* (2007); Liu & Lapusta (2008); Shi *et al.* (2008)). The occurrence of supershear transition has been inferred from observations of large earthquakes. This has been further confirmed in the laboratory (Xia *et al.* (2004), Lu (2009)) and numerical models have been developed to approximately simulate the experiments (Lu *et al.* (2009)).

We numerically model the effects of experimental nucleation procedure using spectral boundary-integral method (BIM). Boundary integral methods have been widely used to investigate spontaneous propagation of cracks in elastic media (e.g., Das (1980); Andrews (1985); Das & Kostrov (1988); Cochard & Madariaga (1994); Lapusta *et al.*

(2000)). Formulations discussed by Perrin *et al.* (1995) and Geubelle & Rice (1995) allowed for 3D dynamic crack propagation in a homogeneous linearly elastic solid. Further formulations of Geubelle & Breitenfeld (1997) and Breitenfeld & Geubelle (1998) extended the earlier formulations and dealt with the problem of dynamic crack propagation on bimaterial interfaces accounting for both tangential and normal displacements of the fracture surface.

One of the approaches to modeling fracture is based on cohesive zone models. The idea of a crack tip cohesive zone was first proposed by Barenblatt (1959). A similar model was suggested by Dugdale (1960) to account for the plastic zone at the crack tip. The physical motivation for postulating a cohesive model is different in different applications but the form of cohesive models is similar in all cases. The fracture is regarded as a gradual process in which the separation is resisted by cohesive tractions. The relationship between the cohesive traction and the opening displacement is governed by a cohesive law. The cohesive zone models used in problems of dynamic crack growth include the cohesive models developed by Camacho & Ortiz (1996) and Xu & Needleman (1994).

The algorithm developed has been tested in the case of the Lamb's problem of step loading on a half space by a concentrated normal force on its boundary. The original formulation of the problem was by Lamb (1904). The numerical solutions were also directly compared with the closed form analytical solutions to the Lamb's problem was given by Pekeris (1955).

1.2 Description of experiments that motivate our modeling

In this section, we describe the experimental setup and techniques developed by Xia (2005) and Lu (2009). The experiment is designed to reproduce the basic physics

governing the rupture dynamics of crustal earthquakes while still preserving enough simplicity to make conclusions by direct observation.

1.2.1 Configuration of the experiment

The experimental setup mimics a fault in the Earth's crust. The crust is simulated by a large Homalite plate of dimensions $150\text{mm} \times 150\text{mm} \times 10\text{mm}$ (Figure 1.1). Relevant properties of Homalite-100 are listed in the Table. 1.1 from Lu (2009). The Homalite plate is cut into two identical quadrilaterals and are put together to introduce a frictional interface. The interface has an inclination angle α with respect to one of the plate edges. The frictional interface is used to simulate a fault. A uniaxial pressure (P) acts uniformly on the top and the bottom ends of the sample. Experimental parameters (P and α) determine the resolved shear traction $\tau = P \sin \alpha \cos \alpha$ and resolved normal traction $\sigma = P \cos^2 \alpha$ along the fault. Varying α allows to vary the nondimensional fault prestress $\tau/\sigma = \tan \alpha$ and study its effects on rupture dynamics and varying P allows for the study of the effect of absolute prestress.

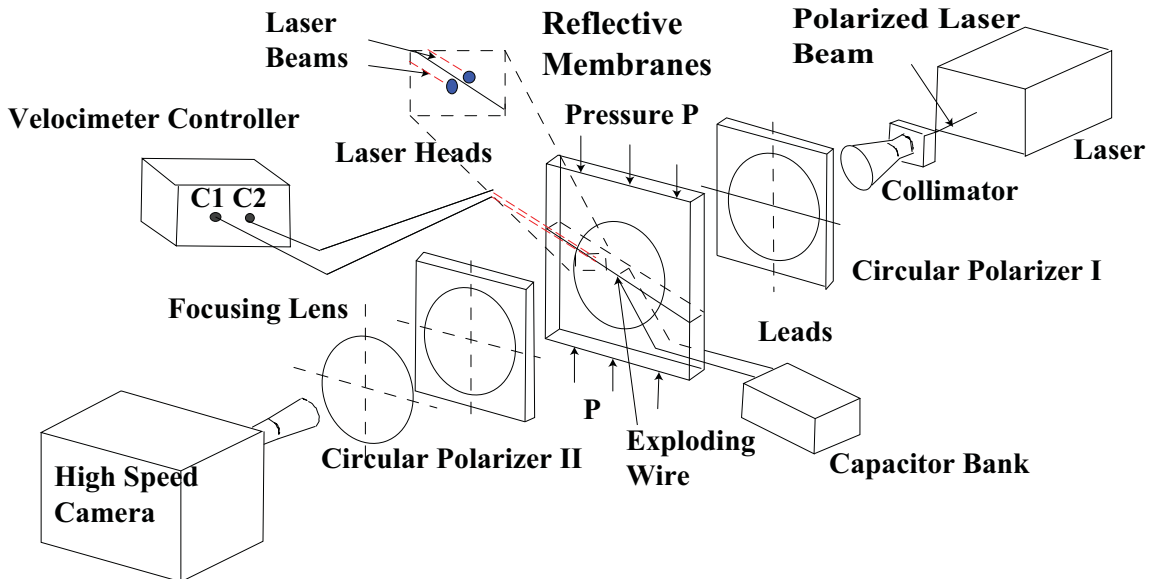


Figure 1.1: Experimental Setup. Adapted from Lu (2009)

Material Property	Homalite-100
Young's modulus E (MPa)	3860
Shear modulus μ (MPa)	1429.63
Shear wave speed c_s (m/s)	1078.10
Dilatational wave speed c_p (m/s) (Plane-strain)	2244.24
Dilatational wave speed c_p (m/s) (Plane-stress)	1891.11
Poisson ratio	0.35
Density ρ (kg/m ³)	1230

Table 1.1: Summary of mechanical properties of Homalite-100

1.2.2 Rupture nucleation mechanism

The triggering of a natural earthquake can be achieved either by increase of the shear loading or by decrease of the fault strength at a specific location. Both mechanisms have been applied in numerical simulations of earthquake rupture dynamics (Andrews (1976); Andrews & Ben-Zion (1997); Cochard & Rice (2000); Aagaard *et al.* (2001)).

In the experiments, the dynamic rupture is initiated by means of explosion of a thin nickel wire as shown in Figure 1.2. A nickel wire with a diameter of 0.08 mm is embedded within a 0.1 mm hole through the thickness of the entire plate. The ends of the wire are connected to a capacitor (15 μ F) that is charged by a high voltage power supply (1-3 kV). Upon closing the switch, the electric energy stored in the capacitor causes a high current in the thin nickel wire for a short duration. The high current turns the nickel wire into high temperature, high pressure plasma. The explosion either changes fault normal pressure to tensile and drives the dynamic rupture as a mixed-mode rupture or reduces it locally and facilitates a pure mode II rupture along the interface.

An order of magnitude estimate for the pressure created by the explosion was given

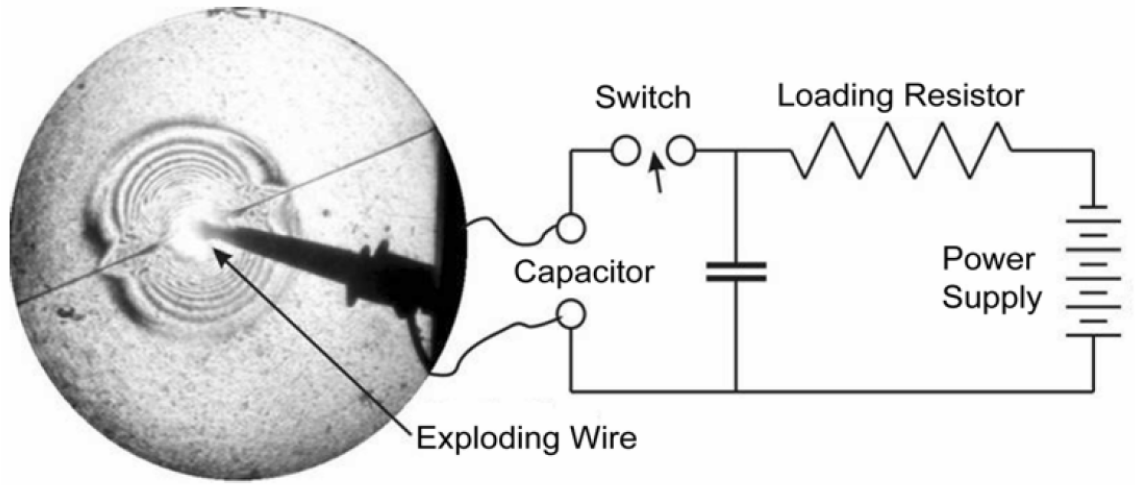


Figure 1.2: Schematic diagram of the exploding wire system coupled with a photoelastic fault model. Adapted from Xia (2005)

by Xia (2005) using the Grüneisen equation of state:

$$p_0 - p_x = \frac{\gamma(v)}{v} (E - E_x) \quad (1.1)$$

where γ is the Grüneisen parameter (approximately 1.88 for Nickel), E and E_x are the total internal energy and cold internal energy, p_0 and p_x are the total pressure and cold pressure and v is the volume of the material. The cold pressure and the cold energy are due to the mechanical interaction of atoms and are negligible. The total energy supplied by the capacitor is

$$E_{total} = \frac{CV^2}{2} \quad (1.2)$$

For a case of $V = 1$ kV, the total energy is 7.5 J. Assuming losses of the order of 1 J due to wire expansion, from (1.1) we can calculate the peak pressure of the order of 10 GPa. In the subsequent chapters we study the effect of the nucleation procedure in further detail.

1.3 Relevant experimental observations

Detailed experiments were conducted by Lu (2009) to understand the nucleation conditions due to the explosion procedure. The diagnostic methods used were dynamic photoelasticity and laser velocimetry. In addition to photoelastic imaging, two laser velocimeters were used to measure the particle velocity histories of two points, one above and one below the fault interface. Experiments were conducted on interfaces of zero inclination and the particle velocities were measured at a distance of 10 mm from the point of explosion. Particle velocities measured included fault-parallel velocity along the interface and fault-normal velocity at a point directly above the point of explosion.

One set of such measurements (Lu (2009)) is shown in Figures 1.3 & 1.4. If the explosion were axisymmetric, the response of both points would be the same but different response was observed during the experiments (Figures 1.3 & 1.4). Thus one could infer the possibility of a mode I crack opening due to explosion.

The aim of this thesis is to extend the existing code for modeling shear ruptures (Lapusta *et al.* (2000), Day *et al.* (2005), Lu *et al.* (2009)) to include the mode I component and to use the developed code and experimental measurements of Lu (2009) to infer parameters of the initiation procedure. These parameters can be used in future studies to model the experimental results on supershear transition (Xia (2005), Lu (2009)) and rupture modes (Lu *et al.* (2007)).

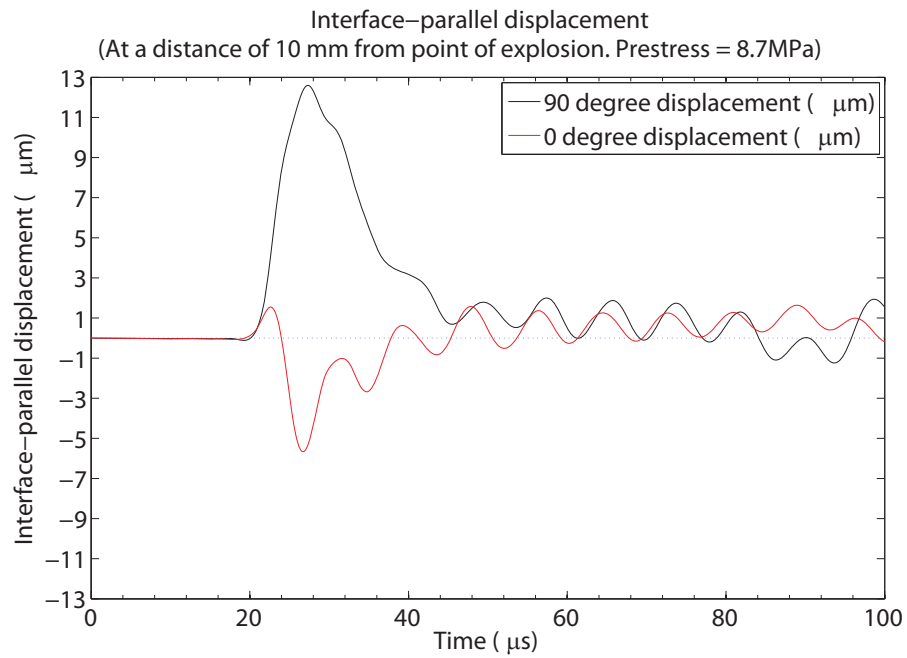


Figure 1.3: Comparison of the experimentally measured interface-parallel displacement for 0-degree and 90-degree points. Adapted from Lu (2009)

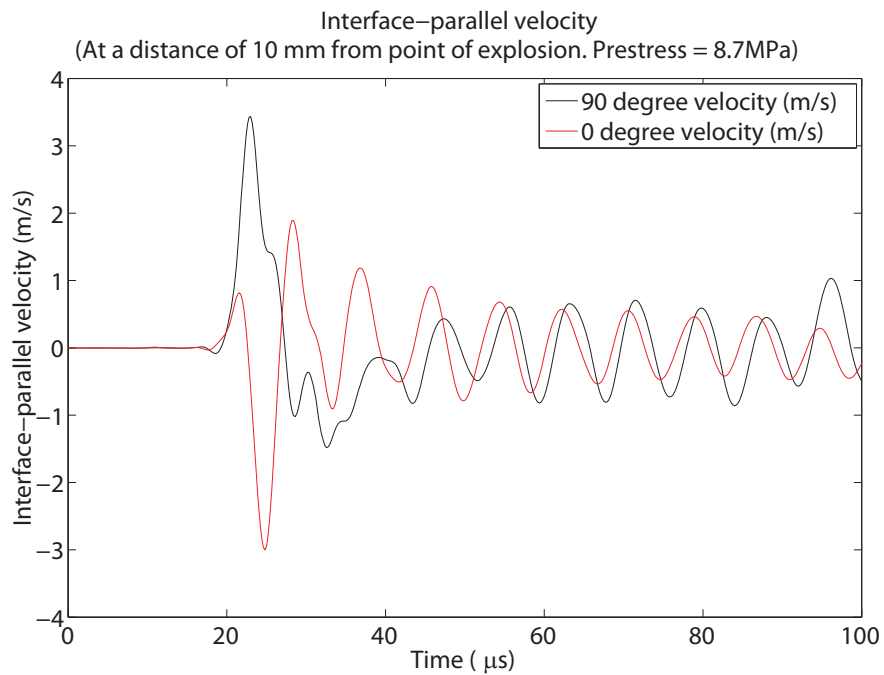


Figure 1.4: Comparison of the experimentally measured interface-parallel velocity for 0-degree and 90-degree points. Adapted from Lu (2009)

Chapter 2

Spectral Boundary Integral Method And Its Numerical Implementation

2.1 Introduction to dynamic fracture simulations

Dynamic fracture mechanics simulations and the problem of spontaneously propagating cracks have been an important area of fracture mechanics research in engineering and geophysics. Dynamic fracture mechanics simulations require high degree of refinement in spatial and temporal discretization to accurately represent the rapid changes in field variables associated with traveling crack tips and elastic waves. On the other hand, large domains of analysis are required to reduce the interactions due to domain boundaries. This results in a substantial challenge in terms of computational cost.

Various numerical techniques have been developed over the years to investigate the problem of spontaneous crack propagation, including finite element and finite difference methods (e.g., Ortiz & Pandolfi (1999), Yu *et al.* (2002), Templeton *et al.*). However both methods incorporate simulation of wave propagation in the bulk, which makes them applicable to problems with heterogeneous bulk but computationally expensive. For dynamic rupture of plane interfaces embedded in a uniform elastic space, boundary integral methods have emerged as the most accurate and efficient choice (e.g. Das (1980), Andrews (1985), Das & Kostrov (1988), Cochard & Madariaga

(1994), Geubelle & Rice (1995), Perrin *et al.* (1995), Ben-Zion & Rice (1997), Geubelle & Breitenfeld (1997), Kame & Yamashita (1999), Aochi *et al.* (2000), Lapusta *et al.* (2000), Lapusta & Rice (2000), Day *et al.* (2005)). The boundary integral method is based on restricting the consideration to the interface plane. The elastodynamic response of the surrounding elastic media is expressed in terms of integral relationships between interface displacements and tractions. These integral relationships involve convolutions of space and time of displacement discontinuities and histories. The histories are obtained through integral relationships between displacement discontinuities and convolution kernels. The convolutions account for the wave propagation and are analytically derived through closed-form Green function. This eliminates the need to simulate the wave propagation through elastic media.

In the study of anti-plane shear study of a slip on a planar fault, Perrin *et al.* (1995) adopted the spectral representation of a slip distribution as a Fourier series in the space coordinate along the fracture plane, instead of dealing with the approximations to the space-time convolution integral, as in standard BIM. In this work, we follow Perrin *et al.* (1995) in adopting the spectral representation of the relation between the tractions and the resulting discontinuities.

The spectral scheme has been developed over the years (Perrin *et al.* (1995); Geubelle & Rice (1995); Geubelle & Breitenfeld (1997); Breitenfeld & Geubelle (1998), Day *et al.* (2005)). It provides an attractive alternative for the simulation of spontaneous crack propagation. The spectral formulation allows one to study in great detail the spontaneous initiation, propagation, and arrest of one or more planar cracks and faults embedded in an infinite medium and subjected to space- and time-varying dynamic loading. It provides a major advantage in comparison with the conventional boundary integral method. The spectral scheme involves a convolution in time as the dynamic stresses are computed in the spectral domain while the conventional scheme involve a triple convolution integral.

2.2 Theoretical formulation of the spectral boundary integral method

The spectral formulation is based on the Fourier representation of stresses and displacements in spatial coordinates along a fracture plane in an infinite, homogeneous, linearly elastic body. The formulation embodies an exact elastodynamic representation of the relation existing between the Fourier coefficients of tractions and corresponding displacement discontinuities. In this section, we give the theoretical formulation of the spectral method for the two-dimensional case following Breitenfeld & Geubelle (1998).

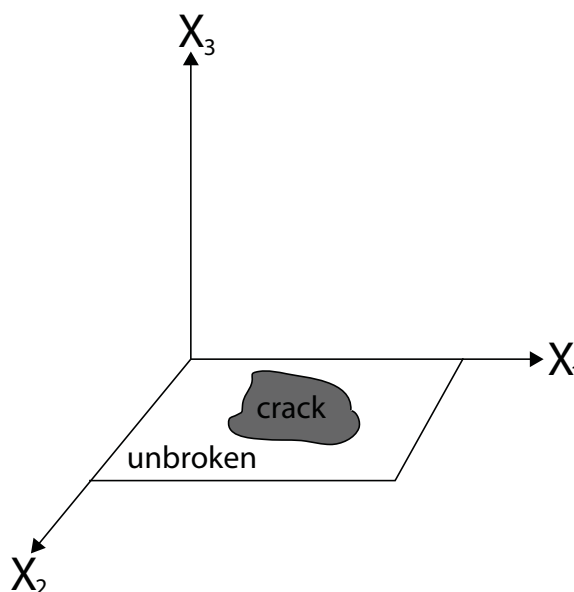


Figure 2.1: Problem Geometry

Let the Cartesian coordinates be defined as shown in Figure 2.1 such that the fracture plane coincides with $x_2 = 0$. Hence x_1 and x_3 are coordinates in the plane and elastodynamic fields will exist in the adjoining half spaces $x_2 > 0$ and $x_2 < 0$.

Considering a 2D formulation, we consider that the displacements and the stress fields solely depend on x_1 and x_2 . Let $\sigma_{ij}(x_1, x_2, t)$ and $u_i(x_1, x_2, t)$ denote the elastodynamic

stress and displacement field, respectively. Let $T_\alpha(t : q)$ and $U_\alpha(t : q)$ denote the q th-mode Fourier coefficients of the in-plane traction stresses and displacements such that:

$$\begin{aligned}\sigma_{2\alpha}(x_1, 0^\pm, t) &= T_\alpha(t; q)e^{iqx_1} \\ u_\alpha^\pm(x_1, 0^\pm, t) &= U_\alpha^\pm(t; q)e^{iqx_1}\end{aligned}\tag{2.1}$$

The first two components of the displacement field $u_i(x_\alpha, t)$ can be expressed as:

$$\begin{aligned}u_1(x_\alpha, t) &= \phi_{,1}(x_\alpha, t) + \psi_{,2}(x_\alpha, t) \\ u_2(x_\alpha, t) &= \phi_{,2}(x_\alpha, t) - \psi_{,1}(x_\alpha, t)\end{aligned}\tag{2.2}$$

where the potentials ϕ and ψ satisfy the wave equations:

$$\begin{aligned}c_d^2\phi_{,\alpha\alpha} &= \phi_{,tt} \\ c_s^2\psi_{,\alpha\alpha} &= \psi_{,tt}\end{aligned}\tag{2.3}$$

while the third displacement component is such that

$$c_s^2u_{3,\alpha\alpha} = u_{3,tt}\tag{2.4}$$

Considering one particular spectral component

$$[\phi(x_\alpha, t), \psi(x_\alpha, t), u_3(x_\alpha, t)] = e^{iqx_1} [\Phi(x_2, t; q), \Psi(x_2, t; q), \Omega(x_2, t; q)]\tag{2.5}$$

Now introducing the Laplace transform, the scalar wave equations (2.3) and (2.4) reduce to:

$$\begin{aligned}\hat{\Phi}''(x_2, p; q) &= q^2\alpha_d^2\Phi(x_2, p; q) \\ \hat{\Psi}''(x_2, p; q) &= q^2\alpha_s^2\Psi(x_2, p; q) \\ \hat{\Omega}''(x_2, p; q) &= q^2\alpha_s^2\Omega(x_2, p; q)\end{aligned}\tag{2.6}$$

where

$$\begin{aligned} (\)' &= \partial/\partial x_2 \\ \alpha_d &= \sqrt{1 + \frac{p^2}{q^2 c_d^2}}, \quad \alpha_s = \sqrt{1 + \frac{p^2}{q^2 c_s^2}} \end{aligned} \quad (2.7)$$

Bounded solutions for (2.6) for $x_2 > 0$ has the form as in (2.8). Similar analogous solution can be derived for $x_2 < 0$.

$$\begin{aligned} \hat{\Phi}(x_2, p; q) &= \hat{\Phi}_0(p; q) e^{-|q| \alpha_d x_2} \\ \hat{\Psi}(x_2, p; q) &= \hat{\Psi}_0(p; q) e^{-|q| \alpha_s x_2} \\ \hat{\Omega}(x_2, p; q) &= \hat{\Omega}_0(p; q) e^{-|q| \alpha_s x_2} \end{aligned} \quad (2.8)$$

Combining the equations (2.2), (2.5) and (2.8), the Laplace-transformed displacement field for the particular mode is given to be:

$$\begin{aligned} \hat{u}_1(x_\alpha, p) &= e^{iqx_1} \left(iq \hat{\Phi}_0(p; q) e^{-|q| \alpha_d x_2} - |q| \alpha_s \hat{\Psi}_0(p; q) e^{-|q| \alpha_s x_2} \right) \\ \hat{u}_2(x_\alpha, p) &= e^{iqx_1} \left(-|q| \alpha_d \hat{\Phi}_0(p; q) e^{-|q| \alpha_d x_2} - iq \hat{\Psi}_0(p; q) e^{-|q| \alpha_s x_2} \right) \\ \hat{u}_3(x_\alpha, p) &= e^{iqx_1} \hat{\Omega}_0(p; q) e^{-|q| \alpha_s x_2} \end{aligned} \quad (2.9)$$

We are concerned with the tractions acting along the fracture plane $x_2 = 0$ and the resulting displacements. Considering the Fourier coefficients as defined in (2.1), relations (2.9) reduce to:

$$\begin{aligned} \hat{U}_1(p; q) &= iq \hat{\Phi}_0(p; q) - |q| \alpha_s \hat{\Psi}_0(p; q) \\ \hat{U}_2(p; q) &= -|q| \alpha_d \hat{\Phi}_0(p; q) - iq \hat{\Psi}_0(p; q) \end{aligned} \quad (2.10)$$

which can be inverted to obtain

$$\hat{\Phi}_0(p; q) = \frac{-iq\hat{U}_1(p; q) + |q|\alpha_s\hat{U}_2(p; q)}{q^2(1 - \alpha_s\alpha_d)} \quad (2.11)$$

$$\hat{\Psi}_0(p; q) = \frac{|q|\alpha_d\hat{U}_1(p; q) + iq\hat{U}_2(p; q)}{q^2(1 - \alpha_s\alpha_d)}$$

Using (2.10) and (2.11) in (2.9), we obtain the solution for the displacement fields $\hat{u}_i(x_\alpha, p)$ for the upper half space in terms of the components $\hat{U}_i(p; q)$ along the upper side $x_2 = 0^+$ of the fracture plane.

$$\begin{aligned} \hat{u}_1(x_\alpha, p) = e^{iqx_1} & \left[\hat{U}_1(p; q) \frac{e^{-|q|\alpha_d x_2} - \alpha_s\alpha_d e^{-|q|\alpha_s x_2}}{1 - \alpha_s\alpha_d} \right. \\ & \left. + \hat{U}_2(p; q) \frac{iq\alpha_s}{|q|(1 - \alpha_s\alpha_d)} (e^{-|q|\alpha_d x_2} - e^{-|q|\alpha_s x_2}) \right] \end{aligned} \quad (2.12)$$

$$\begin{aligned} \hat{u}_2(x_\alpha, p) = e^{iqx_1} & \left[\hat{U}_1(p; q) \frac{iq\alpha_d}{|q|(1 - \alpha_s\alpha_d)} (e^{-|q|\alpha_d x_2} - e^{-|q|\alpha_s x_2}) \right. \\ & \left. + \hat{U}_2(p; q) \frac{e^{-|q|\alpha_s x_2} - \alpha_s\alpha_d e^{-|q|\alpha_d x_2}}{1 - \alpha_s\alpha_d} \right] \end{aligned}$$

Now using (2.1) and (2.12) the Fourier coefficients of the traction components of the two half spaces can be obtained to be:

$$\hat{T}_1(p; q) = \mp \mu^\pm |q| \frac{\alpha_d^\pm (1 - \alpha_s^{\pm 2})}{1 - \alpha_s^\pm \alpha_d^\pm} \hat{U}_1^\pm(p; q) + i\mu^\pm q \left(2 - \frac{1 - \alpha_s^{\pm 2}}{1 - \alpha_s^\pm \alpha_d^\pm} \right) \hat{U}_2^\pm(p; q) \quad (2.13)$$

$$\hat{T}_2(p; q) = -i\mu^\pm q \left(2 - \frac{1 - \alpha_s^{\pm 2}}{1 - \alpha_s^\pm \alpha_d^\pm} \right) \hat{U}_1^\pm(p; q) \mp \mu^\pm |q| \frac{\alpha_d^\pm (1 - \alpha_s^{\pm 2})}{1 - \alpha_s^\pm \alpha_d^\pm} \hat{U}_2^\pm(p; q)$$

Next, we extract the instantaneous responses of the two half-spaces which are given

by:

$$[\hat{T}_1]_{\text{inst}} = \mp \frac{\mu^\pm}{c_s^\pm} p \hat{U}_1^\pm(p; q) \quad (2.14)$$

$$[\hat{T}_2]_{\text{inst}} = \mp \frac{c_d^\pm}{c_s^{\pm 2}} \mu^\pm p \hat{U}_2^\pm(p; q)$$

Now rewriting (2.13) we obtain the expressions for Fourier coefficients of traction components

$$\begin{aligned} \hat{T}_1(p; q) = & -\frac{\mu^\pm}{c_s^\pm} p \hat{U}_1^\pm(p; q) \mp \mu^\pm |q| \left[\frac{\alpha_d^\pm (1 - \alpha_s^{\pm 2})}{1 - \alpha_s^\pm \alpha_d^\pm} - \frac{p}{|q| c_s^\pm} \right] \hat{U}_1^\pm(p; q) \\ & + i \mu^\pm q \left[2 - \frac{1 - \alpha_s^{\pm 2}}{1 - \alpha_s^\pm \alpha_d^\pm} \right] \hat{U}_2^\pm(p; q) \end{aligned} \quad (2.15)$$

$$\begin{aligned} \hat{T}_2(p; q) = & \mp \frac{c_d^\pm}{c_s^\pm} \mu^\pm p \hat{U}_2^\pm(p; q) \mp \mu^\pm |q| \left[\frac{\alpha_s^\pm (1 - \alpha_s^{\pm 2})}{1 - \alpha_s^\pm \alpha_d^\pm} - \frac{c_d^\pm p}{c_s^\pm |q| c_s^\pm} \right] \hat{U}_2^\pm(p; q) \\ & - i \mu^\pm q \left[2 - \frac{1 - \alpha_s^{\pm 2}}{1 - \alpha_s^\pm \alpha_d^\pm} \right] \hat{U}_1^\pm(p; q) \end{aligned}$$

Thus in the space-time domain we have the 2D elastodynamic relations, between the traction components of the stress (τ_α) acting on the fracture plane and the resulting displacements (u_α^\pm), are given by:

$$\tau_1(x_1, t) = \tau_1^0(x_1, t) \mp \frac{\mu^\pm}{c_s^\pm} \frac{\partial u_1(x_1, t)}{\partial t} + f_1^\pm(x_1, t) \quad (2.16)$$

$$\tau_2(x_1, t) = \tau_2^0(x_1, t) \mp \frac{c_d^\pm \mu^\pm}{c_s^\pm c_s^\pm} \frac{\partial u_2(x_1, t)}{\partial t} + f_2^\pm(x_1, t)$$

where $\tau_\alpha^0(x_1, t)$ are the externally applied traction stresses and $f_\alpha^\pm(x_1, t)$ represents the convolution terms corresponding to the last two terms of (2.15).

The Fourier coefficients of the functional are related to the displacement discontinuities through the convolution kernels and are given by

$$\begin{aligned}
F_1(t; q) &= \pm \mu^\pm |q| \int_0^t H_{11}(|q|c_s^\pm t') U_1^\pm(t - t'; q) |q|c_s^\pm dt' \\
&\quad + i(2 - \eta^\pm) \mu^\pm q U_2^\pm(t; q) \\
&\quad + i\mu^\pm q \int_0^t H_{12}(|q|c_s^\pm t') U_2^\pm(t - t'; q) |q|c_s^\pm dt'
\end{aligned} \tag{2.17}$$

$$\begin{aligned}
F_2(t; q) &= \mp \mu^\pm |q| \int_0^t H_{22}(|q|c_s^\pm t') U_2^\pm(t - t'; q) |q|c_s^\pm dt' \\
&\quad - i(2 - \eta^\pm) \mu^\pm q U_1^\pm(t; q) \\
&\quad - i\mu^\pm q \int_0^t H_{12}(|q|c_s^\pm t') U_1^\pm(t - t'; q) |q|c_s^\pm dt'
\end{aligned}$$

where $\eta = c_d/c_s$.

This formulation is known as the ‘‘Displacement Formulation’’ because the convolutions are done on the histories of the Fourier coefficients of displacement discontinuities. To separate the static (long-term) and transient dynamic responses, the integrals in (2.17) are integrated by parts to obtain the Velocity Formulation (Perrin *et al.* (1995)). The Fourier coefficients of the functional in the velocity formulation

are given to be:

$$\begin{aligned}
F_1(t; q) = & \pm \mu^\pm |q| \left[L_{11} U_1^\pm - \int_0^t K_{11}(|q| c_s^\pm t') \dot{U}_1^\pm(t - t'; q) dt' \right] \\
& + i \mu^\pm q \left[L_{12} U_2^\pm - \int_0^t K_{12}(|q| c_s^\pm t') U_2^\pm(t - t'; q) dt' \right] \\
& + i(2 - \eta^\pm) \mu^\pm q U_2^\pm(t; q)
\end{aligned} \tag{2.18}$$

$$\begin{aligned}
F_2(t; q) = & \pm \mu^\pm |q| \left[L_{22} U_2^\pm - \int_0^t K_{22}(|q| c_s^\pm t') \dot{U}_2^\pm(t - t'; q) dt' \right] \\
& + i \mu^\pm q \left[L_{12} U_1^\pm - \int_0^t K_{12}(|q| c_s^\pm t') U_1^\pm(t - t'; q) dt' \right] \\
& - i(2 - \eta^\pm) \mu^\pm q U_1^\pm(t; q)
\end{aligned}$$

The Kernels in Displacement Formulation (H_{11} , H_{12} and H_{22}) are as calculated in Breitenfeld & Geubelle (1998) and the Kernels in Velocity Formulation, K_{11} , K_{12} , K_{22} , are given to be:

$$\begin{aligned}
K_{11} &= L_{11} - \int_0^T H_{11}(\eta) d\eta \\
K_{12} &= L_{12} - \int_0^T H_{12}(\eta) d\eta \\
K_{22} &= L_{22} - \int_0^T H_{22}(\eta) d\eta
\end{aligned} \tag{2.19}$$

where L_{11} , L_{12} and L_{22} are given to be:

$$\begin{aligned} L_{11} &= \int_0^{\infty} H_{11}(\eta) d\eta \\ L_{12} &= \int_0^{\infty} H_{12}(\eta) d\eta \\ L_{22} &= \int_0^{\infty} H_{22}(\eta) d\eta \end{aligned} \tag{2.20}$$

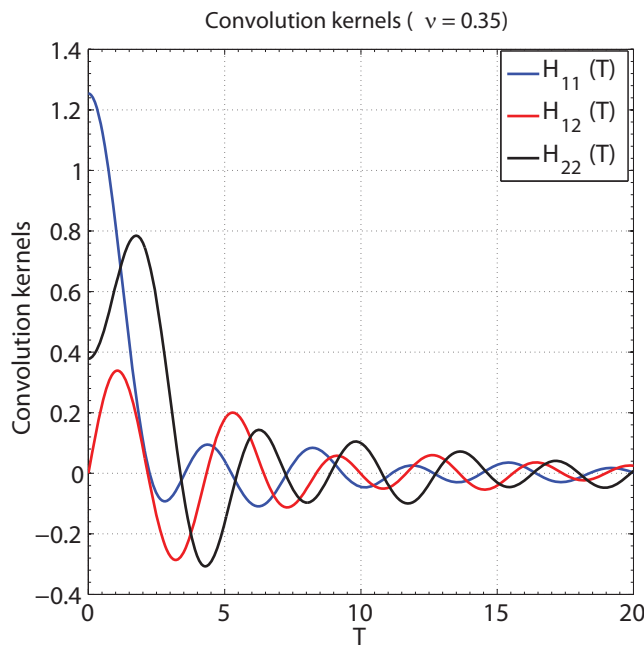


Figure 2.2: Convolution kernels in displacement formulation for a Poisson ratio $\nu = 0.35$

The displacement convolution kernels and velocity convolution kernels are presented in Figure 2.2 and Figure 2.3 respectively for a Poisson's ratio $\nu = 0.35$

2.3 Numerical implementation of the spectral scheme

The implementation of the 2D spectral formulation in this work is based on the developments of Perrin *et al.* (1995), Geubelle & Rice (1995), Breitenfeld & Geubelle

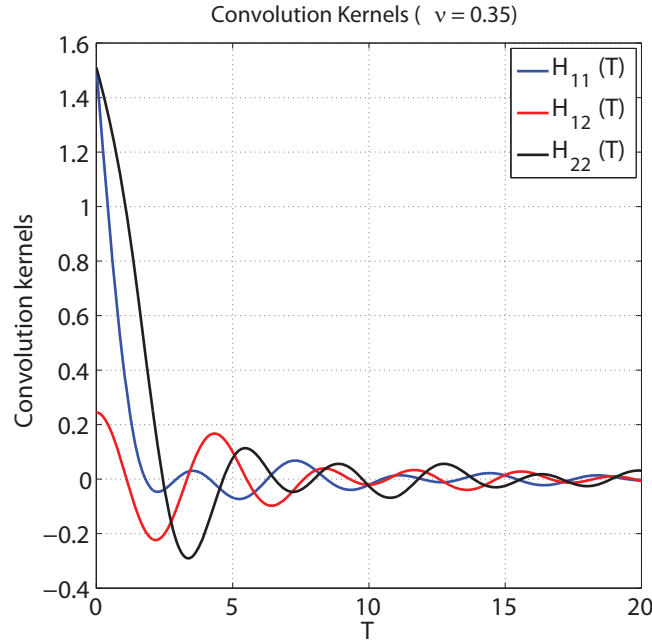


Figure 2.3: Convolution kernels in velocity formulation for a Poisson ratio $\nu = 0.35$

(1998), Day *et al.* (2005) and Liu (2009). It starts by expressing the u_j^\pm and f_j^\pm distributions on the fracture plane as a double Fourier series with period X in the x_1 direction such that

$$\begin{cases} u_j^\pm(x_1, t) \\ f_j^\pm(x_1, t) \end{cases} = \sum_{q=-K/2}^{K/2} \begin{cases} U_j^{k\pm}(t) \\ F_j^{k\pm}(t) \end{cases} e^{2\pi i(\frac{kx_1}{X})} \quad (2.21)$$

A conventional FFT algorithm is used to link spatial and spectral representations, with K sampling points distributed uniformly over the X cells of the fracture plane. Once the convolution term is computed using (2.18) in the spectral domain and transferred back to the spatial domain, (2.16) is used to calculate the updated velocities $\dot{u}_k^\pm(x_1, t)$. This is then integrated in time with an explicit scheme to derive the displacement field.

$$ua_j^\pm(x_1, t + \Delta t) = u_j^\pm(x_1, t) + \Delta t \dot{u}_j^\pm(x_1, t) \quad (2.22)$$

during the first iteration.

$$ub_j^\pm(x_1, t + \Delta t) = u_j^\pm(x_1, t) + 0.5\Delta t (\dot{u}_j^\pm(x_1, t) + ua_j^\pm(x_1, t + \delta t)) \quad (2.23)$$

during the second iteration. ua_j and ub_j represent the displacements from first and second iterations respectively. $\dot{u}a_j$ and $\dot{u}b_j$ represent the velocities from the first and second iterations respectively.

The time step Δt is chosen to be a fraction of time needed for the shear wave to propagate the smallest distance between the grid points defined on the fracture plane as

$$\Delta t = \beta \frac{\Delta x}{\max(c_s^+, c_s^-)} \quad (2.24)$$

The user-defined parameter β plays a critical role in stability and precision of the numerical scheme for the bimaterial code as discussed in Breitenfeld & Geubelle (1998).

Continuity conditions are incorporated along the interface plane and a cohesive failure model is introduced to allow for spontaneous propagation of an interface crack. The failure models discussed in this work are the Camacho-Ortiz Model (Camacho & Ortiz (1996)) and a reversible rate-independent model (Breitenfeld & Geubelle (1998)). The cohesive laws and the theoretical formulation will be discussed in detail in the subsequent sections.

The sequence of operations performed, at each iteration, at each time step is summarized below:

1. Update the displacement distributions u_j^\pm using (2.22) and (2.23).
2. Update the externally applied loads τ_j^0 .
3. Update the interface strength using the cohesive relations.
4. Compute the convolution terms using (2.18) and use a FFT algorithm to link the spatial and spectral domains.
5. Initially we assume that the interface does not undergo further failure and the two half space move together ($\dot{u}_j^+ = \dot{u}_j^- = \dot{u}_j$), i.e. the relative displacements

between the two half space in the normal direction are zero. Under this assumption we compute the resulting interface velocity \dot{u}_j and resulting tractions τ_j^{in} using the relations

$$\dot{u}_1 = \frac{c_s^+}{\mu^+} \left(\frac{f_1^+ - f_1^-}{1 + \frac{\xi}{\zeta}} \right), \quad \tau_1^{in} = \tau_1^0 + f_1^+ - \mu^+ \frac{\dot{u}_1}{c_s^+} \quad (2.25)$$

$$\dot{u}_2 = \frac{c_s^+}{\mu^+} \left(\frac{f_2^+ - f_2^-}{\eta^+ + \frac{\xi}{\zeta} \eta^-} \right), \quad \tau_2^{in} = \tau_2^0 + f_2^+ - \mu^+ \eta^+ \frac{\dot{u}_2}{c_s^+}$$

where $\xi = c_s^+/c_s^-$ and $\zeta = \mu^+/\mu^-$ are the mismatch parameters.

6. Compare the calculated normal component of the interface traction with the normal component of the interface strength given by the cohesive model.
7. If no failure is detected, step (5) is valid.
8. If failure is detected, then the top and the bottom half spaces move at different velocities and the velocities need to be recalculated using

$$\dot{u}_2^+ = \frac{c_s^+}{\mu^+ \eta^+} (\tau_2^0 + f_2^+ - \tau_n^{str}) \quad (2.26)$$

$$\dot{u}_2^- = \frac{\zeta c_s^+}{\xi \mu^+ \eta^-} (\tau_n^{str} - \tau_2^0 - f_2^-)$$

9. In the region where the crack surfaces move independently, check for possible overlapping by computing the predicted normal crack opening displacement (COD).

$$\delta_2^{pred} = u_2^+ - u_2^- + \Delta t (\dot{u}_2^+ - \dot{u}_2^-)$$

10. If the predicted COD is negative, then the local motion of the crack surface is

modified to ensure a vanishing COD and a continuity of normal traction.

$$\dot{u}_2^+ = \frac{c_s^+}{\eta^+ + \frac{\xi\eta^-}{\zeta}} \left[\frac{\tau_2^0 + f_2^+ - \tau_2^0 - f_2^-}{\mu^+} - \frac{\xi\eta^-}{\zeta} \left(\frac{u_2^+ - u_2^-}{c_s^+ \Delta t} \right) \right]$$

$$\dot{u}_2^- = \dot{u}_2^+ + \frac{u_2^+ - u_2^-}{\Delta t} \quad (2.27)$$

$$\tau_2 = \tau_2^0 + f_2^+ - \eta^+ \mu^+ \frac{\dot{u}_2^+}{c_s^+}$$

11. However the interface could close under a compressive stress. In such a case, the velocities are recalculated using (2.26) and checked for penetration of the two half space using (2.27).
12. Finally the knowledge of the normal compressive stresses can be used in conjunction with a Coulomb friction model to introduce a frictional resistance to the relative motion in shear of the fracture surfaces. Cases with frictional sliding are not considered in this work, but mixed mode crack propagation with friction is a goal for future work.

This concludes the description of the algorithm used in this work. Further results and conclusions are discussed in the subsequent chapters.

2.4 Theoretical formulation of cohesive zone laws

In the cohesive zone model approach, fracture is regarded as a gradual process in which the separation is resisted by cohesive tractions. The relation between the cohesive traction and the opening displacement is governed by a cohesive law. Some of the cohesive zone models used in dynamic rupture simulations include those developed by Xu & Needleman (1994) and Camacho & Ortiz (1996). In this section we discuss

Ortiz-Camacho cohesive zone model and Reversible rate-independent cohesive zone model.

2.4.1 Ortiz-Camacho Model

In this section we discuss the cohesive law proposed by Camacho & Ortiz (1996). This cohesive law accounts for the tension-shear coupling through the introduction of an effective scalar opening displacements. The form of effective opening displacement allows for different weights to be applied to the normal and tangential components of the opening displacement vector. The cohesive behavior of the material is assumed to be rigid, or perfectly coherent, up to the attainment of an effective traction, at which point the cohesive surface begins to open. The cohesive law is rendered irreversible by assumption of linear unloading to the origin.

An effective opening displacement δ , which assigns different weights to the normal δ_n and sliding δ_s displacements such that

$$\delta = \sqrt{\beta^2 \delta_s^2 + \delta_n^2}, \quad \delta_n = \delta \cdot \hat{n}, \quad \delta_s = \delta \cdot \hat{t} \quad (2.28)$$

The Ortiz-Camacho cohesive zone model assumes that the fracture process is irreversible in nature and accounts for the damage in the material. The cohesive forces which resist opening and sliding weaken irreversibly with increasing crack opening displacement. When the velocity changes sign, the cohesive forces are ramped down to zero as the opening displacement diminishes to zero. The tensile cohesive relation is as shown in Figure 2.4.

In the tensile case, when the normal opening displacement δ_σ increases monotonically, the cohesive stress (σ) are ramped down linearly as a function of δ_σ (Figure 2.4). The cohesive tractions reduce to zero at critical opening displacement $\delta_\sigma = \delta_{\sigma cr}$ and remain zero upon further opening or closing. This forms a new surface and the cohesive tractions vanish.

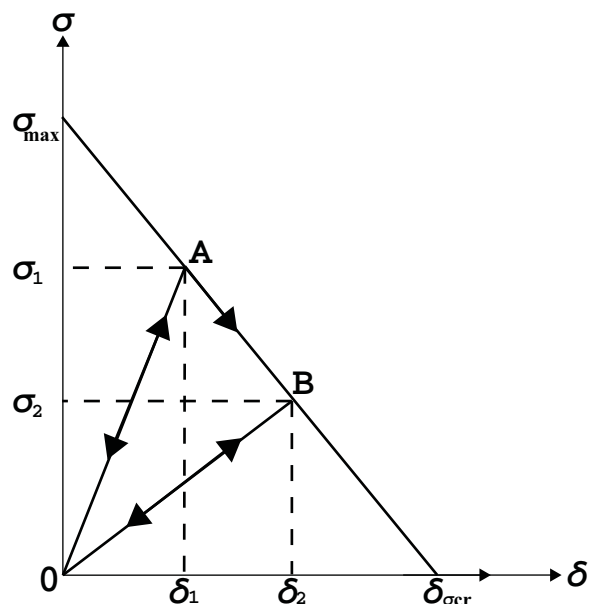


Figure 2.4: Tensile cohesive relation - Ortiz-Camacho cohesive relation

However since in the laboratory earthquake experiments, an interface already exists, the cohesive traction is completely due to cohesion between the two half spaces. Also since no new surface is being formed and the opening is small, we can assume that the surface is not irreversibly damaged due to the increasing crack opening displacement.

2.4.2 Reversible rate-independent cohesive model

In this section we discuss reversible rate-independent cohesive model. The rate-independent cohesive model is similar to the Camacho-Ortiz model discussed earlier except that it does not take into account the irreversible effects due to damage.

In the laboratory dynamic rupture experiments the damage can be considered negligible. Also since an already interface exists, new surface is not formed during the rupture as assumed in the cohesive law in Camacho & Ortiz (1996). Hence the opening and closing modes can be considered reversible and without permanent set. The reversible rate-independent cohesive model related the opening tractions (τ_n) and

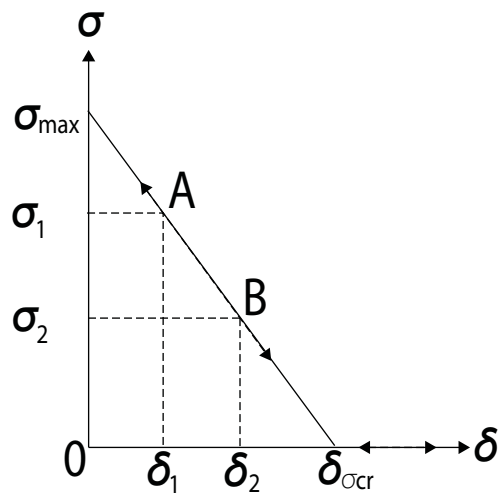


Figure 2.5: Reversible rate-independent cohesive model

the opening displacement (δ_n). The reversible rate-independent cohesive model is as shown in Figure 2.5.

When the normal opening displacement δ_σ increases monotonically, the cohesive stress σ is ramped down linearly as a function of δ_σ . The cohesive tractions reduce to zero at critical opening displacement $\delta_\sigma = \delta_{\sigma cr}$. When the velocity changes sign and the interface begins to close, the cohesive is linearly ramped up to maximum strength of the interface.

Chapter 3

Validation of the developed numerical approach

3.1 Study of Lamb's problem on an elastic half-space

The numerical algorithm developed has been validated using the test case of a Lamb's problem on an elastic half space. The problem is to determine the motion of the surface of a uniform elastic half-space produced by the application of a point force pulse varying with time like the Heaviside unit function. The original problem was proposed by Lamb (1904). Closed form analytical solutions were derived for the Lamb's problem by Dix (1954) and Pekeris (1955).

3.1.1 Theoretical formulation of Lamb's problem

In this section, we discuss briefly the closed form analytical solutions derived for the Lamb's problem (Pekeris (1955)). Let us consider a cylindrical coordinate system. The variation of the normal force (p_{zz}) on the surface with time is represented by the Heaviside unit function $H(t)$ and its spatial localization is such that it is everywhere zero, except at the origin of coordinates where it becomes infinite in such a manner

that:

$$2\pi \int_0^{\infty} p_{zz}(r)r dr = Z \quad (3.1)$$

where Z is a negative constant. The horizontal and the vertical displacements are given to be Lamb (1904):

$$\begin{aligned} q &= \phi_r + \chi_{rz} \\ w &= \phi_z + \chi_{zz} - k^2\chi \end{aligned} \quad (3.2)$$

where the subscripts denote partial differentiation, and the potentials ϕ and χ satisfy the wave equations for educational and equivoluminal motion respectively:

$$\begin{aligned} \nabla^2\phi - h^2\phi &= 0 \\ \nabla^2\chi - k^2\chi &= 0 \end{aligned} \quad (3.3)$$

where $h^2 = \frac{p^2}{c_p^2}$, $k^2 = \frac{p^2}{c_s^2}$, $c_s^2 = \frac{\mu}{\rho}$, $c_p^2 = \frac{\lambda+2\mu}{\rho} = 3c_s^2$. c_p represents the p-wave speed, c_s represents the s-wave speed, p denotes the $\frac{\partial}{\partial t}$. λ and μ are the elastic constants of the medium.

The surface being traction free, both normal and shear stresses reduce to zero. The shear stress p_{rz} and the normal stress p_{zz} are given by

$$\begin{aligned} p_{rz} &= \mu \left(\frac{\partial}{\partial t} \right) (2\phi_z + 2\chi_{zz} - k^2\chi) = 0 \\ p_{zz} &= \lambda h^2\phi + 2\mu (\phi_{zz} + \chi_{zz} - k^2\chi_z) = 0 \end{aligned} \quad (3.4)$$

The actual vertical displacement, $w(r, z, t)$ can be obtained by performing the integration over the Bromwich contour.

$$w(r, z, t) = \frac{1}{2\pi i} \int_{a-i\infty}^{a+i\infty} \left(\frac{e^{pt}}{p} \right) w(r, z, t) dp \quad (3.5)$$

Solving for the actual form of $w(r, z, t)$ (Pekeris (1955)) we have the operational

expression for the vertical displacement in the case of a surface source to be given by the integral

$$w(p) = \frac{Zk^2}{2\pi\mu} \int_0^\infty J_0(\xi r) \xi \alpha \left[(2\xi^2 + k^2)^2 - 4k^2 \xi^2 \alpha \beta \right]^{-1} d\xi \quad (3.6)$$

where $\alpha = \frac{(\xi^2 + h^2)^{\frac{1}{2}}}{k}$ and $\beta = \frac{(\xi^2 + k^2)^{\frac{1}{2}}}{k}$

A closed form solution has been derived for rocks (Poisson' ratio (ν) = 0.25) for the 3-D case by Pekeris (1955). The expressions for the vertical displacement ($w(x_1, t)$) of the interface for $\nu = 0.25$, assuming a traction-free boundary, are given to be:

$$w(x_1, t) = \begin{cases} 0 & \text{if } \tau < 1/\sqrt{3} \\ -\frac{Z}{32\pi\mu x_1} \left[6 - \frac{\sqrt{3}}{\sqrt{\tau^2 - \frac{1}{4}}} - \frac{\sqrt{3\sqrt{3}+5}}{\sqrt{\frac{3}{4} + \frac{\sqrt{3}}{4} - \tau^2}} + \frac{\sqrt{3\sqrt{3}-5}}{\sqrt{\frac{\sqrt{3}}{4} - \frac{3}{4} + \tau^2}} \right] & \text{if } 1/\sqrt{3} < \tau < 1 \\ -\frac{Z}{16\pi\mu x_1} \left[6 - \frac{\sqrt{3\sqrt{3}+5}}{\sqrt{\frac{3}{4} + \frac{\sqrt{3}}{4} - \tau^2}} \right] & \text{if } 1 < \tau < \frac{1}{2}\sqrt{3 + \sqrt{3}} \\ -\frac{3Z}{8\pi\mu x_1} & \text{if } \tau > \frac{1}{2}\sqrt{3 + \sqrt{3}} \end{cases} \quad (3.7)$$

where $\tau = c_s t / x_1$ is the reduced time and x_1 is the distance to the point of application of the force.

3.1.2 Numerical investigation of Lamb's problem

The spectral boundary integral algorithm developed has been tested using the Lamb's problem of step loading on a half space. In addition to the fact that it allows direct comparison with closed form analytical solutions, this also provides the opportunity

to visualize the distinctive effects of dilatational, shear and Rayleigh waves.

The numerical simulation was performed on a square domain $[0, X]$ by $[0, X]$ using a 600 by 600 spatial discretization, so that $\Delta x_1 = \Delta x_3 = X/600$, and a value of $\beta = c_s \Delta t / \Delta x_1 = c_s \Delta t / \Delta x_3 = 0.25$. The point load was applied at the center of the square by assigning $\tau^0 = P / \Delta x_1 \Delta x_3$ at that node and $\tau^0 = 0$ elsewhere.

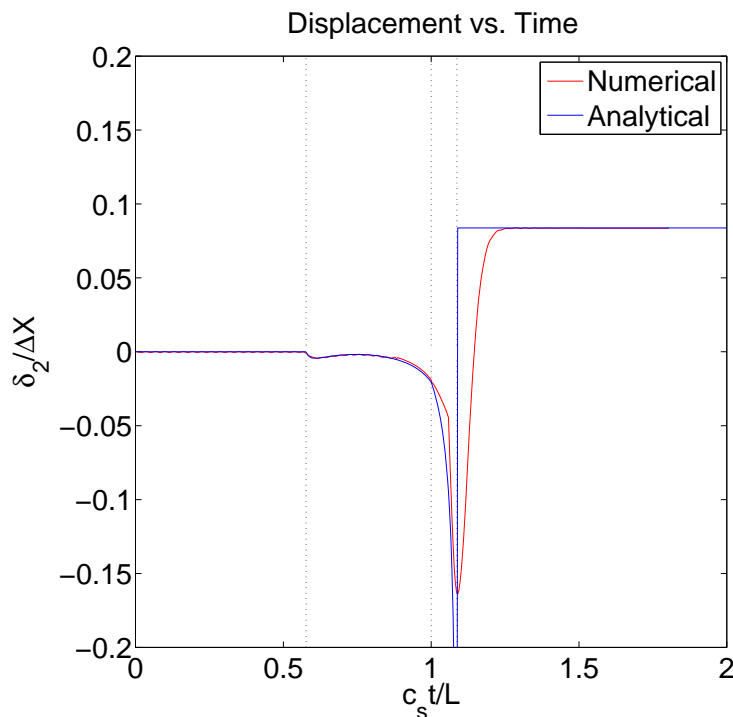


Figure 3.1: Evolution of displacement normal to the traction-free surface at a point located at a distance L from the point of application of load. Dotted lines denote the arrival times of dilatational, shear and Rayleigh waves.

A direct comparison is presented in Figure 3.1 and it illustrates the evolution of the displacement component u_2 normal to the free surface at a distance of 64 elements away from the point of application of force. We can observe a good agreement between the two solutions. The numerical scheme is also able to capture the arrival of dilatational, shear and Rayleigh waves. The solution shows spurious numerical oscillations of small amplitude prior to and at the arrival of the dilatational wave. These oscillations are associated with the truncated spectral representation. Further

at the arrival of the Rayleigh wave, the numerical computed crack opening smoothes out and experiences a Gibbs effect before settling down to the final constant value. This effect is attributed to the discrete Fourier representation of the fields which are unable to capture a discontinuity.

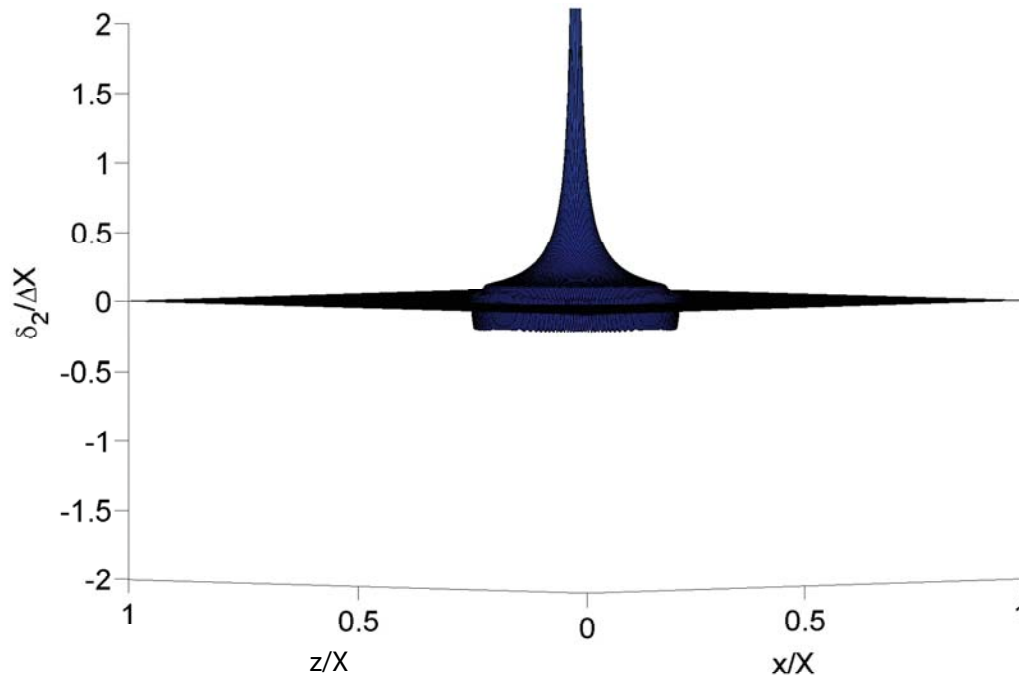


Figure 3.2: Displacement field on the surface of the half space after 200 time steps, showing the concentric waves expanding from the point of application of point load

Figure 3.2 shows the three-dimensional view of the displacement field after 200 time steps. It clearly shows the dilatational precursor which creates the small displacement in the direction opposite to that of the applied force, the singular Rayleigh wave expanding radially from the point of application of force and the $1/r$ singularity after the passage of various waves.

In summary, we find that the numerical results match the theoretical closed-form analytical solution for the Lamb's problem of step loading on an elastic half space.

3.2 Propagating mode-I crack in a plate

There are four length scales in dynamic rupture simulations.

1. The macroscopic scale L characterizes the geometry of the body.
2. The critical crack size ($2L_c$) is the length of the crack at equilibrium. Upon any further loading, the crack becomes unstable and grows rapidly.
3. The cohesive zone length (l_z) is the measure of the length over which the cohesive constitutive relation plays a role.
4. The mesh size Δx provides a non-physical length scale. It is necessary that Δx is smaller than all the physical scales 1-3 for the mesh to provide an accurate resolution.

3.2.1 Critical crack length

In this section we review the procedure adopted by Griffith (1920) to computing the critical crack length by considering a body with an internal crack and which is subjected to external loads as shown in Figure 3.3.

According to the law of conservation of energy, the work performed per unit time by the applied loads (\dot{W}) must be equal to the rates of change of the internal elastic energy (\dot{U}_E), plastic energy (\dot{U}_P), kinetic energy (\dot{K}) of the body, and the energy per unit time ($\dot{\Gamma}$) spent in increasing the crack area.

$$(\dot{W}) = (\dot{U}_E) + (\dot{U}_P) + (\dot{K}) + (\dot{\Gamma}) \quad (3.8)$$

where a dot over the letter refers to differentiation with respect to time.

Since all the changes with respect to time are caused by changes in crack size, we have

$$\frac{\partial}{\partial t} = \frac{\partial}{\partial A} \frac{\partial A}{\partial t} = \dot{A} \frac{\partial}{\partial A} \quad (3.9)$$

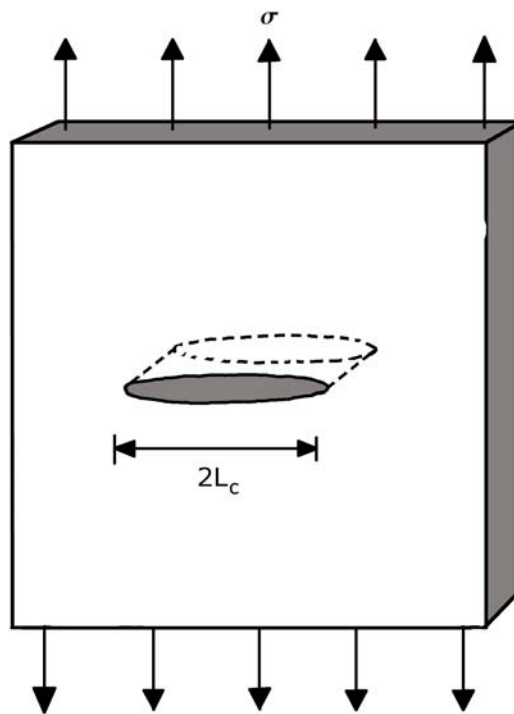


Figure 3.3: A funnel crack in a plate subjected to external loads.

where A represents the crack area, and is equal to $2L_cB$ for the system shown in Figure. 3.3. B represents the thickness of the plate and \dot{A} denotes the crack surface area growth rate per unit time. Thus (3.8) can be rewritten to be

$$-\frac{\partial \Pi}{\partial t} = \frac{\partial K}{\partial t} + \frac{\partial U_P}{\partial t} + \frac{\partial \Gamma}{\partial t} \quad (3.10)$$

where $\Pi = U_E - W$ is the potential energy of the system. Thus (3.10) indicates that the reduction of potential energy is equal to the energy dissipated in kinetic energy, plastic work and surface creation.

However considering a perfectly brittle solid, the energy dissipated in plastic deformation is negligible and can be ignored, i.e. $U_P = 0$. Since the energy spent in increasing the crack area is independent of the crack size, (3.10) can be written as

$$-\frac{\partial \Pi}{\partial t} = \frac{\partial K}{\partial t} + \frac{\partial \Gamma}{\partial t} = \frac{\partial K}{\partial t} + 2\gamma \quad (3.11)$$

where γ represents the surface energy, i.e. energy required to form unit new material surface area or open an interface to separate the two surfaces. The factor 2 represents the two new material surfaces formed or material surface separated during the crack growth.

Now considering an equilibrium crack of size L_c , $\frac{\partial K}{\partial t} = 0$. Thus (3.11) reduces to:

$$-\frac{\partial \Pi}{\partial t} = \frac{\partial \Gamma}{\partial t} = 2\gamma \quad (3.12)$$

where $A = 2L_cB$ for the cracked system shown in Figure 3.3. The above equilibrium equation means that sufficient potential energy must be available to overcome the surface energy of the material.

Griffith (1920) used the stress analysis of Inglis (1913) to show that

$$\Pi = \Pi_0 - \frac{\pi\sigma_0^2 L_c^2 B}{E} \quad (3.13)$$

where Π_0 is the potential energy of the uncracked plate and σ_0 is the external loading. Since the formation of a crack requires the creation of two new surfaces, Γ is given by

$$\Gamma = 4L_c B \gamma \quad (3.14)$$

Thus we have

$$-\frac{\partial \Pi}{\partial A} = \frac{\pi\sigma_0^2 L_c}{E} \quad (3.15)$$

$$\frac{\partial \Gamma}{\partial A} = 2\gamma \quad (3.16)$$

Equating (3.15) and (3.16) and solving for the critical crack size $2L_c$ we have

$$2L_c = \frac{2E\gamma}{\pi\sigma_0^2} \quad (3.17)$$

The surface energy can be given to be $\gamma = \frac{1}{2}\sigma_{max}\delta_{scr}$ and $E = 2\mu(1 + \nu)$. Thus we have the critical crack length to be given by:

$$2L_c = \frac{2\mu(1 + \nu)\sigma_{max}\delta_{scr}}{\pi\sigma_0^2} \quad (3.18)$$

3.2.2 Cohesive zone length

In this section we review the procedure adopted by Rice (1980) to derive the cohesive zone length for a body with an internal crack and which is subjected to external loads as shown in Figure 3.3.

As discussed in Muskhelishvili (1975), for a single crack lying between $-a$ and $+a$

the cohesive zone length is given by

$$\frac{d\delta l_z(x)}{dx} = -\frac{2(1-\nu)}{\pi G\sqrt{a^2-x^2}} \int_{-a}^{+a} \frac{\sqrt{a^2-s^2}\delta\sigma(s)}{x-s} ds - \frac{D}{\pi\sqrt{a^2-x^2}} \quad (3.19)$$

The stress intensity factor at the crack tips $\pm a$ are given to be

$$K = \frac{1}{\sqrt{\pi a}} \int_{-a}^{+a} \sqrt{\frac{a\pm x}{a\mp x}} \delta\sigma(x) dx \pm \frac{GD}{2(1-\nu\sqrt{\pi a})} \quad (3.20)$$

Solving the above nonlinear integral equations as in Rice (1980) for a non-propagating crack, i.e. the crack velocity is zero we have the cohesive zone length to be given to be

$$l_z = \frac{9\pi}{32} \left(\frac{E}{1-\nu^2} \right) \frac{2\gamma}{\sigma_{max}^2} \quad (3.21)$$

For the system in Figure 3.3 the surface energy γ can be given to be $\gamma = \frac{1}{2}\sigma_{max}\delta_{\sigma cr}$ and $E = 2\mu(1+\nu)$. Thus we have that the cohesive zone length of a crack propagating at 0^+ speeds is given by:

$$l_z = \frac{9\pi}{16} \left(\frac{\mu}{1-\nu} \right) \frac{\delta_{\sigma cr}}{\sigma_{max}} \quad (3.22)$$

The cohesive zone length decreases as the crack velocity increases.

3.2.3 Numerical resolution

L_c is relevant for the cohesive-zone models of cracks in situations when the cohesive zone sizes at the crack tips of quasi-static cracks are small compared to the overall crack size, which means that cracks are still quasi-static when opening exceeds $\delta_{\sigma cr}$ over most of the length.

It is important to numerically resolve the cohesive zone and the critical crack length. Both cohesive zone length (l_z) and critical crack size ($2L_c$) need to be discretized by certain number of cells to accurately predict the crack propagation. The discretiza-

$\bar{\sigma}^0 = \frac{\sigma_0}{\sigma_{max}}$	0.33	0.25	0.20	0.08
$N_c = L_c/\Delta x$	100	100	100	800
$l_z/\Delta x$	65.79	37.01	23.68	30.31

Table 3.1: Numerical resolution of critical crack length and cohesive zone length for various levels of prestress

tion in this work has been done as described in Day *et al.* (2005) and Liu & Lapusta (2008) and the numerical discretization has been described in Table 3.1.

The rupture propagation is simulated on a uniform grid with the cell size $\Delta x = L_c/N_c$ and constant time step $\Delta t = \Delta x/(\beta c_s)$. N_c is the number of cells in L_c and β determines the time step as a fraction of time for the shear wave to travel through Δx . The β chosen in the present work is 4 based on the stability study done by Breitenfeld & Geubelle (1998).

This completes the theoretical formulation for the various length scales in dynamic rupture simulations. In the subsequent sections we discuss the results of mode I crack propagation.

3.2.4 Numerical simulation of propagating mode I crack in rocks

In this section we discuss the results obtained by numerical simulation of mode I crack propagation on a bonded interface as shown in Figure 3.3. The plate is made of rocks (Poisson ratio $\nu = 0.25$, density $\rho = 2670 \text{ kg/m}^3$ and shear wave speed $c_s = 2887 \text{ m/s}$). In these simulations we consider Ortiz-Camacho cohesive model with $d_c = 1.3\mu\text{m}$. The rupture is initiated by application of load over the critical

crack size.

The dynamic fracture is simulated on a domain of 30 mm in length. The cohesive strength of the bonded interface is assumed to be 20 MPa. The rupture is simulated for the prestress level of 0.33. The critical crack size ($2L_c$) is calculated to be 10.8 mm and the cohesive zone length (l_z) is calculated to be 3.4 mm. Both the critical crack size and the cohesive zone are resolved as described for a prestress level of 0.33 in the earlier section.

The loading is applied on the critical crack size ($2L_c$) for the entire duration of the simulation ($60\mu s$). The loading profiles that are applied on the critical crack size are:

1. Loading Profile 1: $6.6 + t$ MPa
2. Loading Profile 2: $6.6 + 10 \times t$ MPa
3. Loading Profile 3: $6.6 + H(t)$ MPa
4. Loading Profile 4: $6.6 + 10 \times H(t)$ MPa

where t is the time in μs .

The interface normal and interface parallel displacements, velocities and stresses are recorded for the entire duration of the simulation.

The results of the simulations for the first $8\mu s$ are as shown in Figure 3.4-3.7. For each of the four conceptual loading profiles we observe a propagating mode I crack. As theoretically expected, when the loading applied on the critical crack size is a step function, the particle velocities and the crack tip velocities are higher than when the loading applied on the critical crack size is more gradual.

Once the crack starts to propagate as in Figure 3.5 and Figure 3.6 the crack gradually accelerates to the Rayleigh wave speed, which is the theoretical speed limit for a propagating mode I crack. As can be seen in Figure 3.6, the crack tip for the

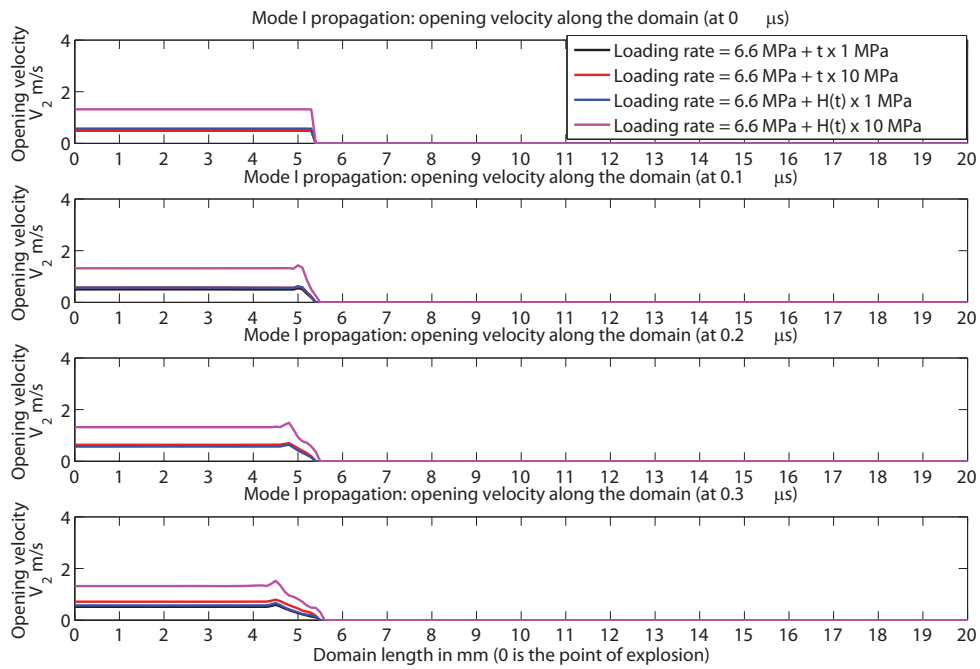


Figure 3.4: Propagation of mode I crack across the domain with time (0, 0.10, 0.20, 0.30 μs)

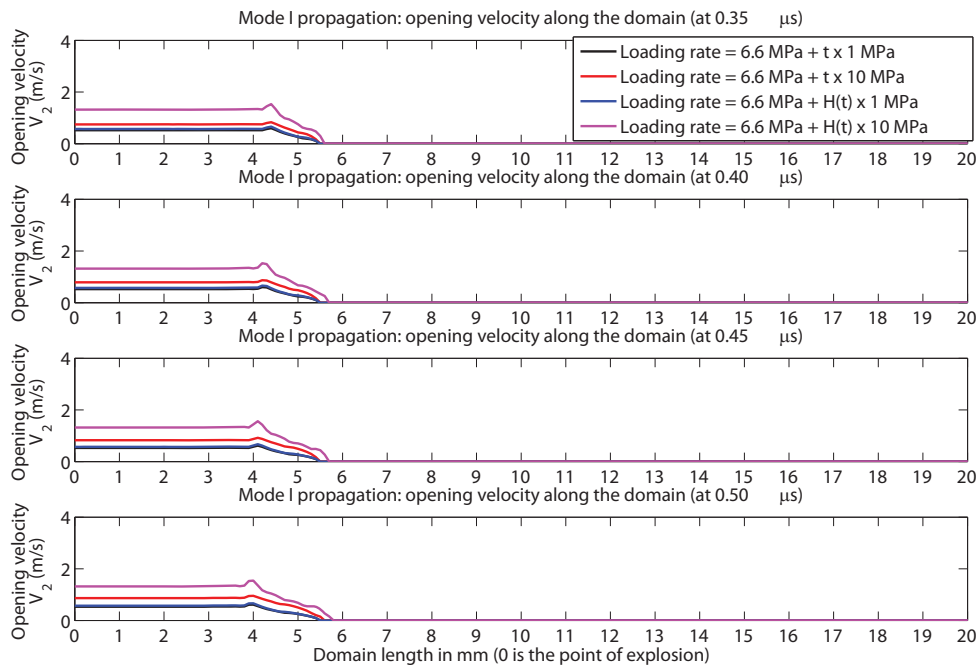


Figure 3.5: Propagation of mode I crack across the domain with time (0.35, 0.40, 0.45, 0.50 μs)

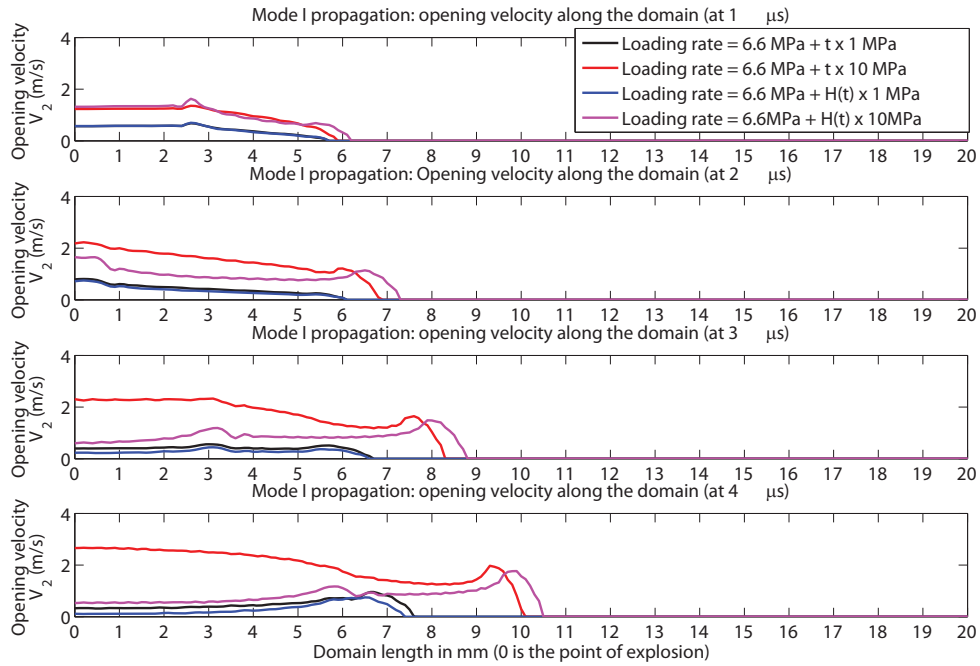


Figure 3.6: Propagation of mode I crack across the domain with time (1, 2, 3, 4 μs)

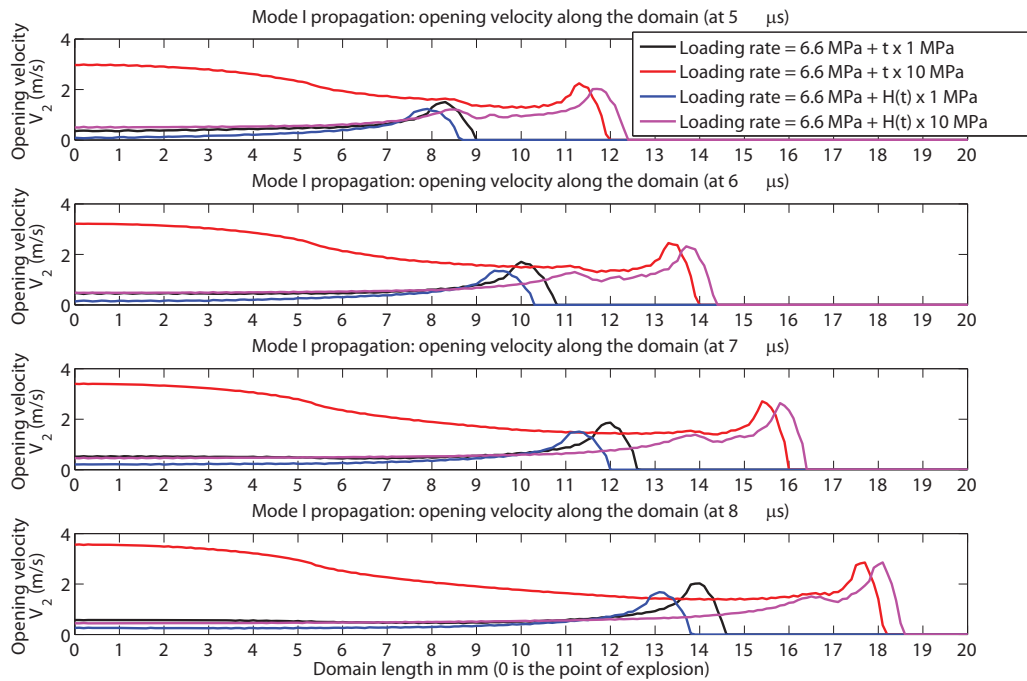


Figure 3.7: Propagation of mode I crack across the domain with time (5, 6, 7, 8 μs)

loading rates of $6.6 \text{ MPa} + t \times 10 \text{ MPa}$ and $6.6 \text{ MPa} + H(t) \times 10 \text{ MPa}$, traveled about 2 mm between $5 - 6 \mu\text{s}$, i.e the average crack tip velocity is about 2000 m/s. Similarly for the loading rates of $6.6 + H(t) \text{ MPa}$ and $6.6 + t \text{ MPa}$, between $5 - 6 \mu\text{s}$ the crack tip is traveled about 1.8 mm, i.e. the average crack tip speed is 1800 m/s. The Rayleigh wave speed in rocks is 2654m/s.

Thus in this section we have shown that our approach can simulate the propagation of a mode I crack along a bonded interface for various loading profiles and also the acceleration of the crack tip speed to the Rayleigh wave speed. In the subsequent section we discuss the mode I crack propagation due to the explosion nucleation used in dynamic rupture experiments.

Chapter 4

Simulations of nucleation procedure in laboratory earthquake experiments

In this chapter we simulate the nucleation conditions of the laboratory dynamic rupture experiments. The triggering mechanism in the experiments is an explosion of a nickel wire in the middle of the interface. During the experiments, a bright flash was observed by Xia (2005) and Lu (2009) for about $5\mu\text{s}$ and this bright flash is attributed to the wire explosion process (heating up of the nickel wire, conversion of the wire to plasma, cooling down of the plasma). They also observed a region of metallic particles deposited on the interface of about 5 to 15 mm in size. This deposition is believed to be due to spreading of plasma along the interface.

Experiments were conducted by Lu (2009) to study the process of electrical wire explosion. Interface parallel displacements and velocities were recorded at a distance of 10 mm from the point of explosion. Also the particle displacements and velocities were measured at a point 10 mm directly above the point of explosion. Lu (2009) observed that the two points showed different behavior as shown in Figure 1.3 and 1.4. In this chapter, we model the nucleation process and compare the interface-parallel displacements obtained numerically and experimentally.

4.1 Comparison of numerically computed and experimentally measured interface-parallel displacements

We numerically simulate the explosion process using conceptual loading profiles and study the effect on the interface-parallel velocities at 10 mm from the point of explosion. The dynamic rupture events are simulated on an interface of 150 mm length using plane stress approximation. Compressive far-field stress of 8.7 MPa is applied. The explosion is simulated using conceptual pressure profiles, as described below, initially over a length of 0.1 mm at the center of the interface. The interface-parallel velocities and displacements are recorded at a distance of 10 mm from the point of explosion. Thus obtained interface-parallel displacements are compared with the experimental results of measurement of interface-parallel velocities by Lu (2009) for a range of parameters of simulated nucleation procedure.

Note that we use a plane stress approximation to model an experiment that has 3D effects. In the experiments the width of the plate is 10 mm and the measurements are done at 10 mm from the explosion site. The oscillatory nature of the measurement (Figures 1.3 & 1.4) is due to the plate thickness and 3D free surface effect (Lu (2009)) and cannot be matched by the modeling. Hence here we are looking for an order of magnitude fit between the numerical and experimental results.

In the numerical model, the cohesive tractions and displacements are related by a cohesive relation. We use both Ortiz-Camacho cohesive zone model and reversible rate-independent cohesive zone model. The maximum cohesive strength of the interface is considered to be 1 MPa and the critical crack opening displacement is 5 μm .

The loading profile used to simulate the explosion process is shown in Figure 4.1. That is the profile of pressure that would act over the 0.1 mm explosion site if the

interface were constrained against any opening. As the loading causes a mode I crack, we recompute the pressure and the region of its application as follows.

The cross-sectional area of the notch in which the nickel wire is embedded is given by

$$A_{wire} = \pi r^2,$$

where $r = 0.1$ mm.

As the interface opens, the pressure due to the plasma acts on all or part of the interface that has opened. The recomputed pressure is given by

$$P = \frac{(P_{explosion} \times \pi r^2)}{A},$$

where A is the area of the opened crack to which the plasma has spread plus the area of the initial notch. A is given by

$$A = \int_{-C_{pl}t}^{C_{pl}t} \delta_2 dx + \pi r^2,$$

where C_{pl} is the speed of plasma propagation and δ_2 is the opening of the interface.

4.1.1 Effect of the explosion pressure

In this section we access the effect of parameter P_{max} on the interface-parallel displacements. The experimental results of Lu (2009) of interface-parallel displacements are compared with the numerical results of interface-parallel displacements at a distance of 10 mm from the point of explosion, $P_{max} = 1, 2, 3, 4, 10$ GPa, and with plasma speed C_{pl} the same as the crack tip speed. The interface-parallel displacements are studied for two time-dependence of the loading profile given in Table 4.1. Figure 4.2 compares the interface-parallel displacements at 10 mm from the point of explosion for loading profile 1 and Ortiz-Camacho cohesive zone model. Figure 4.3 compares

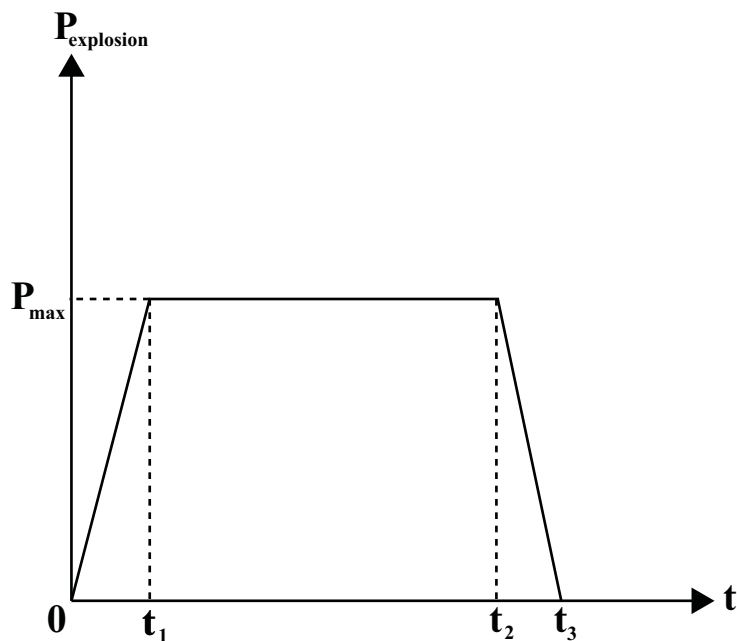


Figure 4.1: The pressure profile used to model the explosion. P_{max} is the maximum pressure. t_1 , t_2 and t_3 are the time parameters of the loading profile.

Loading profile	Time parameter	Plasma speed
Loading profile 1	$t_1 = 0\mu, t_2 = t_3 = 5\mu s$	same as crack speed
Loading profile 2	$t_1 = 1\mu, t_2 = 4\mu, t_3 = 5\mu s$	same as crack speed

Table 4.1: Summary of loading parameters used to study the effect of P_{max}

the interface-parallel displacements at 10 mm from the point of explosion for loading profile 1 and reversible rate-independent cohesive zone model. Figure 4.4 compares the interface-parallel displacements for loading profile 2 and Ortiz-Camacho cohesive zone model. Figure 4.5 is for loading profile 2 and reversible rate-independent cohesive zone model.

Based on Figures 4.2-4.5, we conclude that P_{max} should be of the order of 10 GPa to fit the amplitude of the experimentally measured displacements. This is the same value as the theoretically calculated value of explosion pressure by Xia (2005). We also

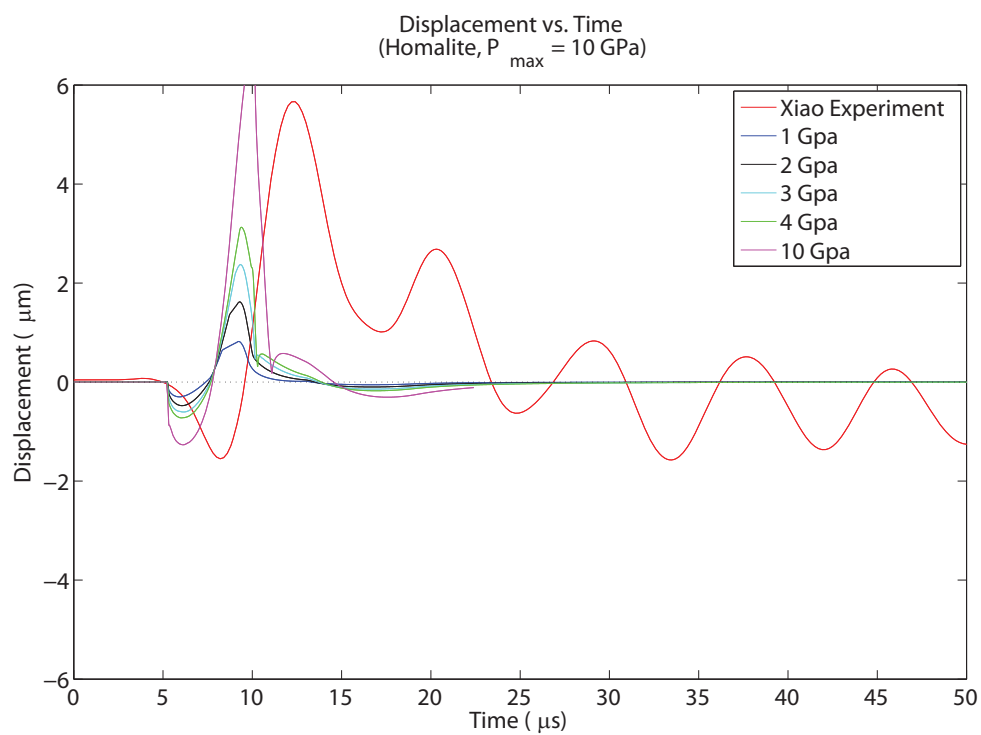


Figure 4.2: Comparison of interface-parallel displacement at a distance of 10 mm from the point of explosion for loading profile 2 and parameters $P_{\max} = 1, 2, 3, 4, 10 \text{ GPa}$ and $t_1 = 0 \mu$, $t_2 = t_3 = 5 \mu$ s. The numerical simulation being governed by Ortiz-Camacho cohesive zone model.

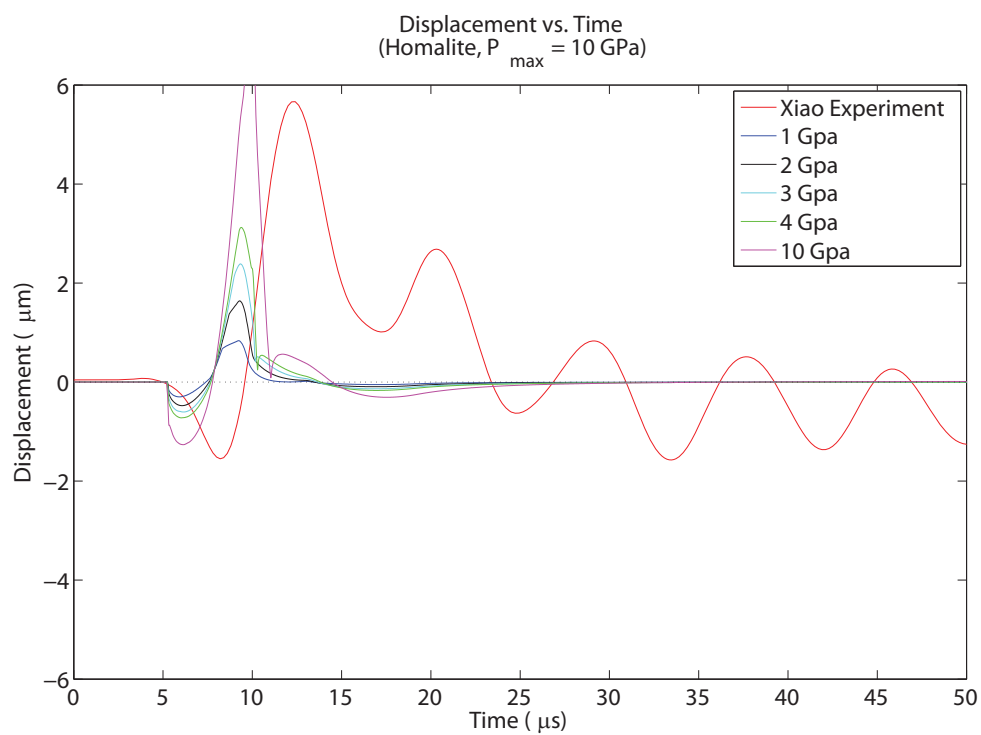


Figure 4.3: Comparison of interface-parallel displacement at a distance of 10 mm from the point of explosion for loading profile 2 and parameters $P_{\max} = 1, 2, 3, 4, 10$ GPa and $t_1 = 0\mu$, $t_2 = t_3 = 5\mu\text{s}$. The numerical simulation being governed by reversible rate-independent cohesive zone model.

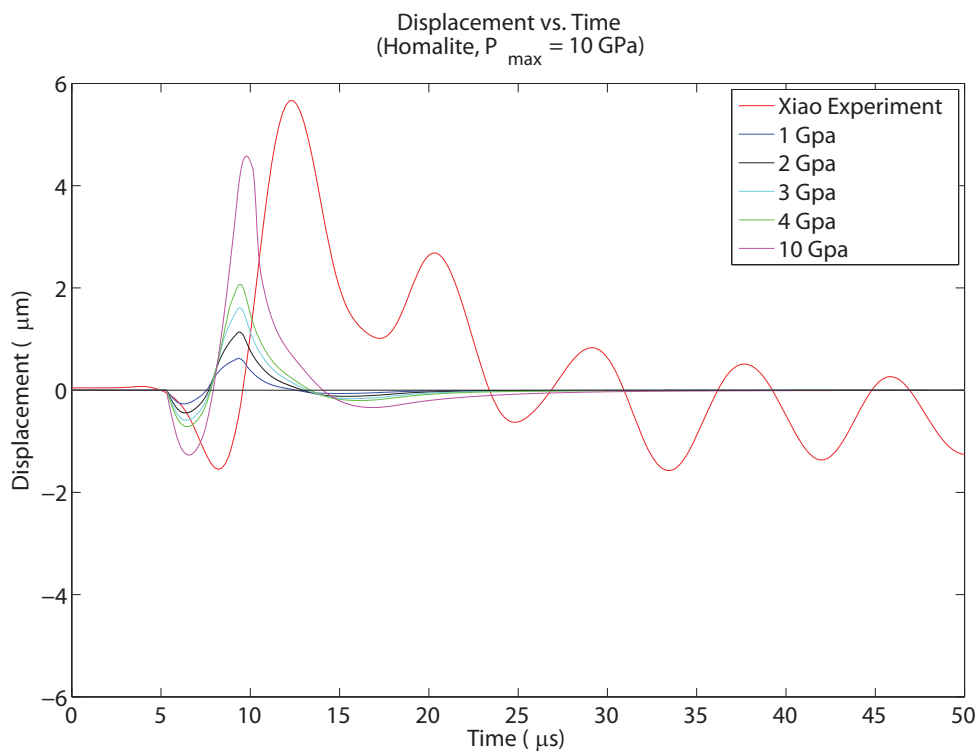


Figure 4.4: Comparison of interface-parallel displacement at a distance of 10 mm from the point of explosion for loading profile 2 and parameters $P_{\max} = 1, 2, 3, 4, 10 \text{ GPa}$ and $t_1 = 0\mu$, $t_2 = 4\mu\text{s}$, $t_3 = 5\mu\text{s}$. The numerical simulation being governed by Ortiz-Camacho cohesive zone model.

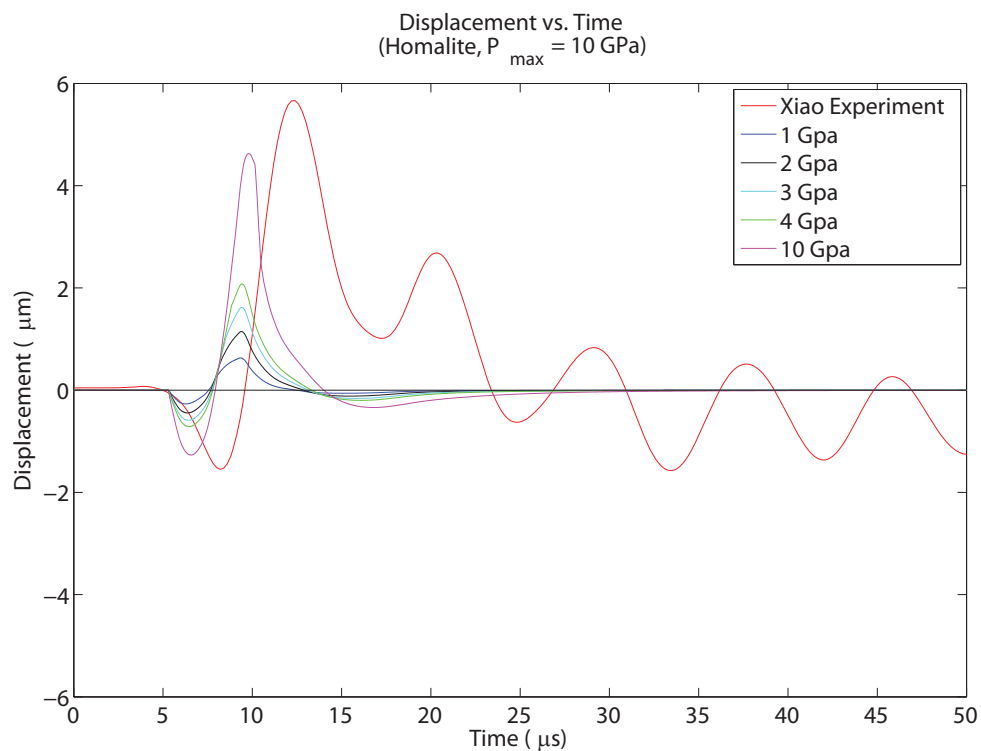


Figure 4.5: Comparison of interface-parallel displacement at a distance of 10 mm from the point of explosion for loading profile 2 and parameters $P_{max} = 1, 2, 3, 4, 10$ GPa and $t_1 = 0\mu$, $t_2 = 4\mu\text{s}$, $t_3 = 5\mu\text{s}$. The numerical simulation being governed by reversible rate-independent cohesive zone model.

observe that the arrival time for the dilatational wave matches between the numerical simulations and the experiments. However, the total width of the displacement pulse is smaller than observed in the experiments.

4.1.2 Effect of the cohesive zone models

In this section, we discuss the effect of the cohesive zone models. From Figures 4.6 and 4.7, we observe that both cohesive zone relations result in nearly identical histories of interface-parallel displacements.

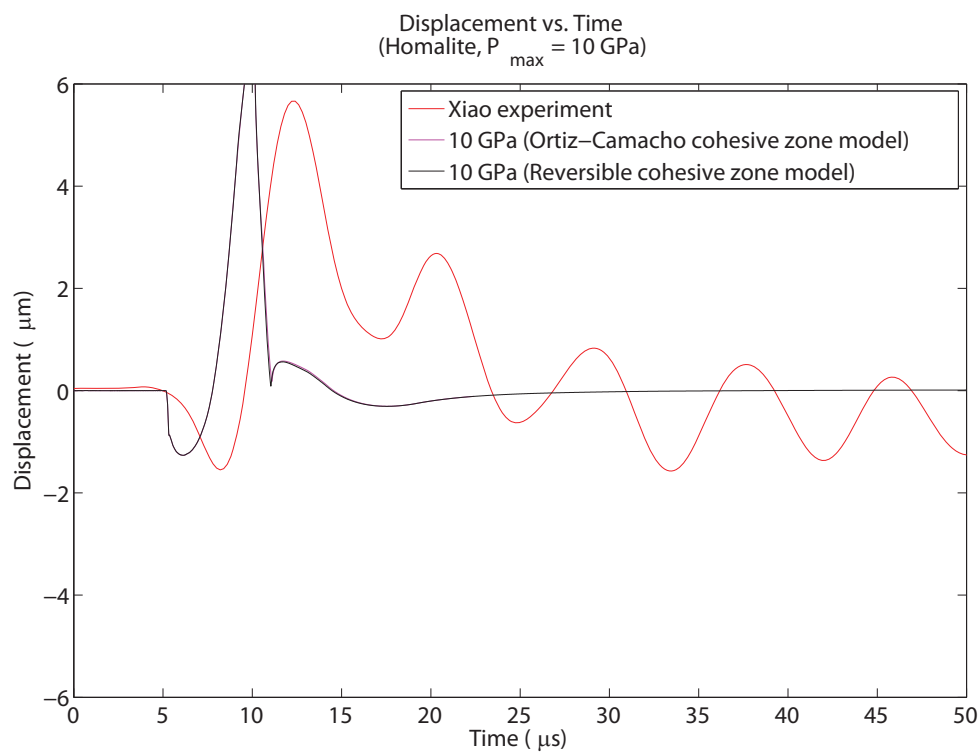


Figure 4.6: Comparison of interface-parallel displacement, for numerical simulations governed by Ortiz-Camacho cohesive zone model and reversible rate-independent cohesive zone model, at a distance of 10 mm from the point of explosion for loading profile 1 with parameters $P_{\max} = 10 \text{ GPa}$ and $t_1 = 0\mu$, $t_2 = t_3 = 5\mu\text{s}$.

Ortiz-Camacho cohesive zone model and reversible rate-independent cohesive zone model have identical behavior except during closing and reopening of the interface.

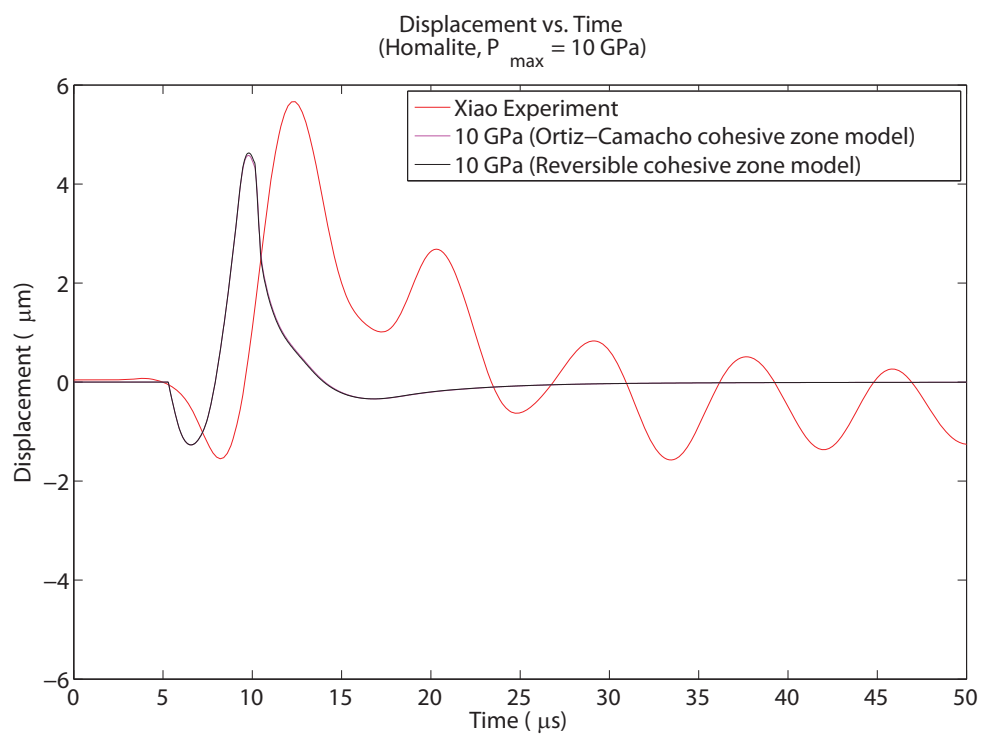


Figure 4.7: Comparison of interface-parallel displacement, for numerical simulations governed by Ortiz-Camacho cohesive zone model and reversible rate-independent cohesive zone model, at a distance of 10 mm from the point of explosion for loading profile 2 with parameters $P_{\max} = 10$ GPa and $t_1 = 0\mu$, $t_2 = 4\mu\text{s}$, $t_3 = 5\mu\text{s}$.

According to Ortiz-Camacho cohesive zone model, the cohesive tractions are reduced linearly to zero during closing and the cohesive tractions are revamped from zero during reopening. According to the reversible rate-independent cohesive zone model, the cohesive tractions increase to the maximum cohesive strength of the interface during closing and the cohesive tractions decreases linearly from maximum cohesive strength of the interface to zero during reopening. In the experiments, the existence of a far-field compressive loading does not allow for the reopening of the interface. The difference in the behavior during closing will be discussed in the next section during the discussion of the propagating mode I crack. Hence this configuration of the experiment causes the two cohesive laws considered to have nearly identical effect.

4.1.3 Effect of loading duration

In this section we discuss the effect of time parameter t_1 , t_2 and t_3 . First, here we study the effect of time parameter t_1 . From Figure 4.8 we conclude that variation in time parameter t_1 has an effect on the width and amplitude of the displacement profile.

Based on Figure 4.8, we conclude that t_1 of $2 \mu\text{s}$ gives the best fit to the experimentally measured displacement profile.

Next we discuss the effect of time parameter $t_2 - t_1$, keeping $t_1 = 2\mu\text{s}$. From Figure 4.9 we conclude that variation in time parameter $t_2 - t_1$ has an effect on the amplitude of the displacement profile.

Based on Figure 4.9, we conclude that $t_2 - t_1$ between $3\text{-}5 \mu\text{s}$ provides a similar fit to the width and amplitude of the displacement pulse.

Based on the results presented so far, we conclude that, for the loading profile considered and with the plasma spreading speed the same as the crack tip speed, the best-fitting loading parameters are $P_{\text{max}} = 10 \text{ GPa}$, $t_1 = 2\mu\text{s}$, $t_2 - t_1 = 4\mu\text{s}$ and $t_3 - t_2 = 1\mu\text{s}$. This best match is shown in Figure 4.10. Note that as discussed in the

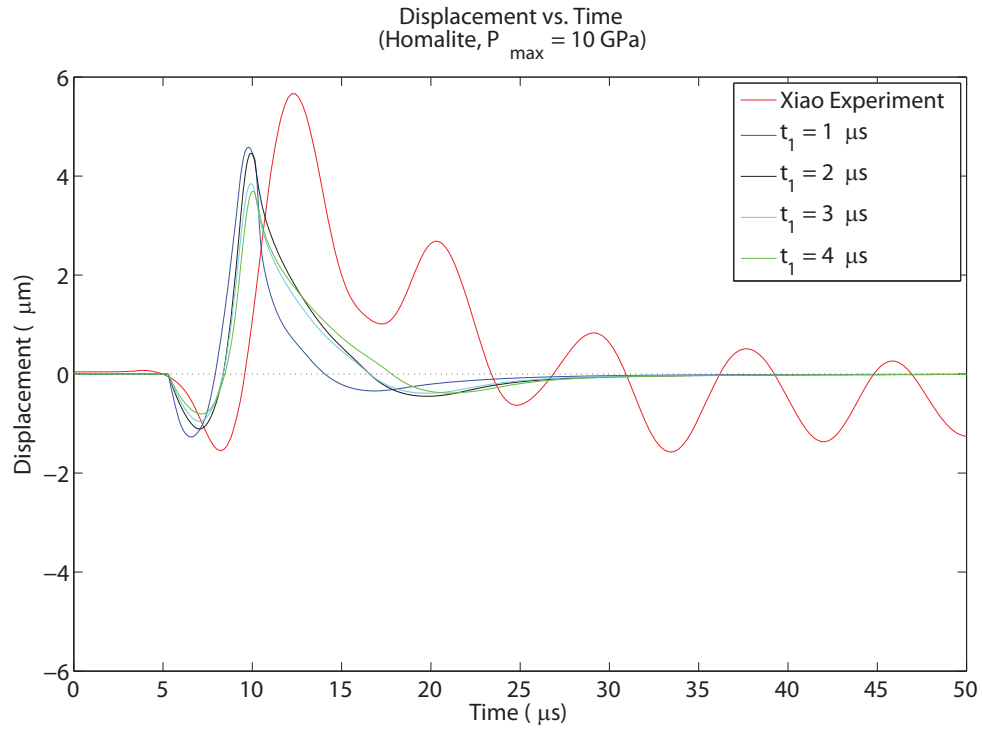


Figure 4.8: Comparison of interface-parallel displacement, for numerical simulations governed by Ortiz-Camacho cohesive zone model, at a distance of 10 mm from the point of explosion for loading profile 1 with parameters $P_{\max} = 10 \text{ GPa}$ and $t_1 = 1, 2, 3, 4 \mu$, $t_2 - t_1 = 3 \mu\text{s}$ and $t_3 - t_2 = 1 \mu\text{s}$.

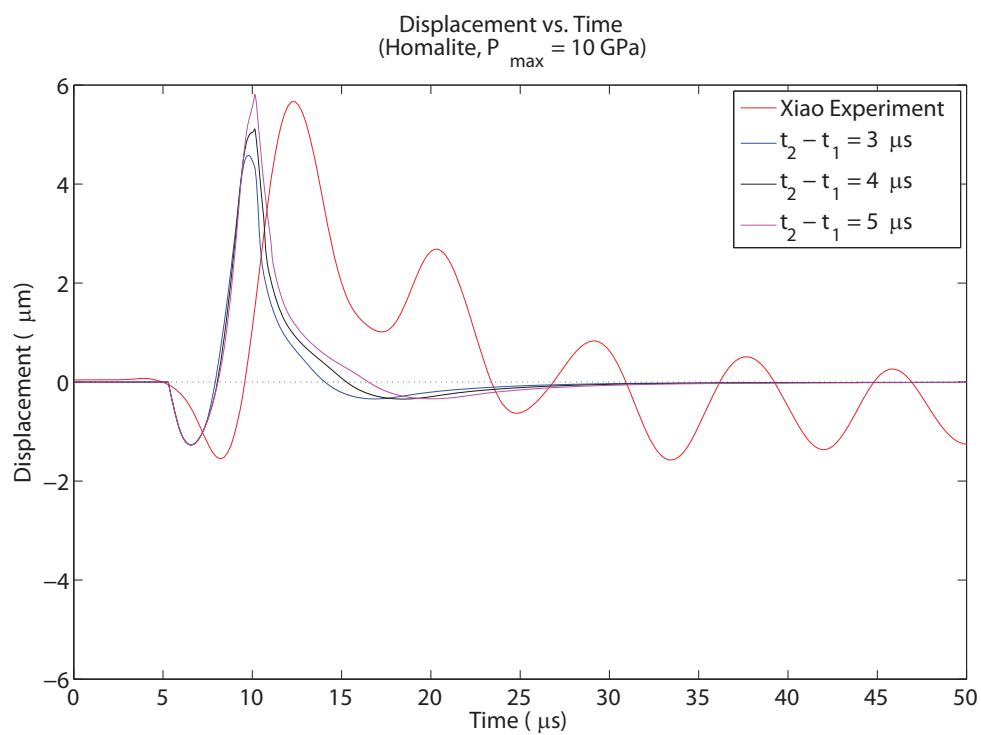


Figure 4.9: Comparison of interface-parallel displacement, for numerical simulations governed by Ortiz-Camacho cohesive zone model, at a distance of 10 mm from the point of explosion for loading profile 1 with parameters $P_{\max} = 10$ GPa and $t_1 = 2 \mu$, $t_2 - t_1 = 3, 4, 5 \mu\text{s}$ and $t_3 - t_2 = 1 \mu\text{s}$.

earlier section we do not expect a perfect fit due to the 3D effects.

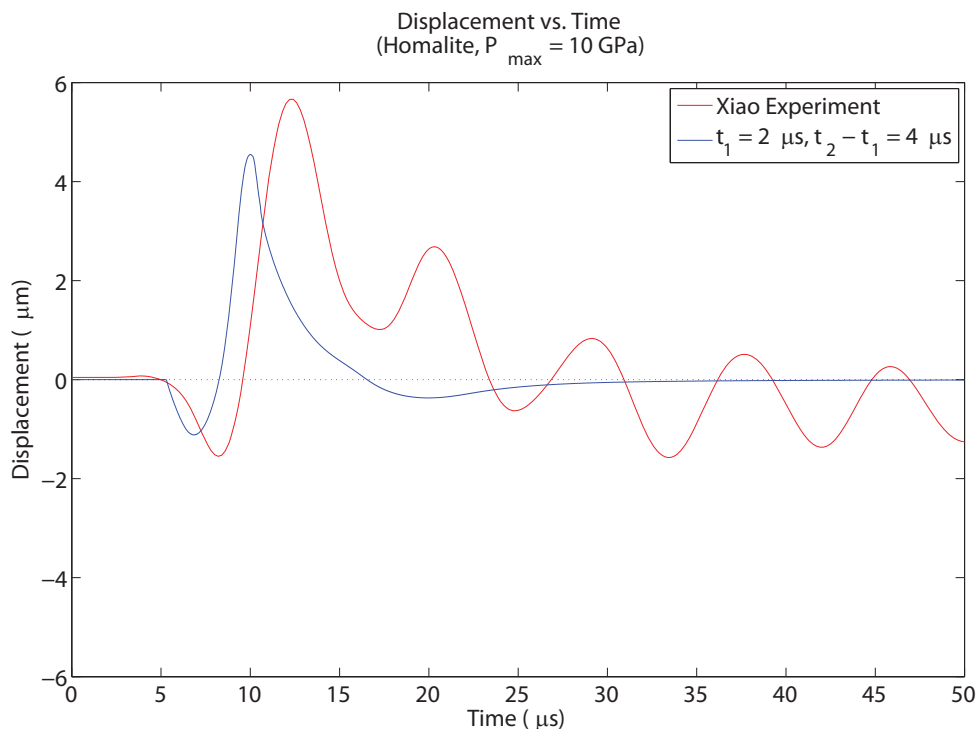


Figure 4.10: The best match between the simulations and the experimental results. The parameters used are $P_{\max} = 10 \text{ GPa}$, $t_1 = 2 \text{ } \mu\text{s}$, $t_2 - t_1 = 4 \text{ } \mu\text{s}$, $t_3 - t_2 = 1 \text{ } \mu\text{s}$ and $C_{\text{pla}} = \text{crack tip speed}$.

4.1.4 Effect of plasma spreading speed (C_{pla})

In the previous sections we assumed that the plasma from the wire explosion expands fast enough to fill the entire opening crack. In this section, we assume that the plasma spreading speed is less than the crack tip speed. We compare the results with three plasma spreading speeds, $C_{\text{pla}} = 250 \text{ m/s}$, 340 m/s , 500 m/s . The results are shown in Figure 4.11. We find that the amplitude of the displacements decreases, but the width of the displacement pulse increases for smaller C_{pla} . Hence the best-fitting nucleation parameters may not involve slower-moving plasma. The detailed study of this phenomenon including the physical modeling of how fast the plasma can spread inside the propagating cracks is left for future work.

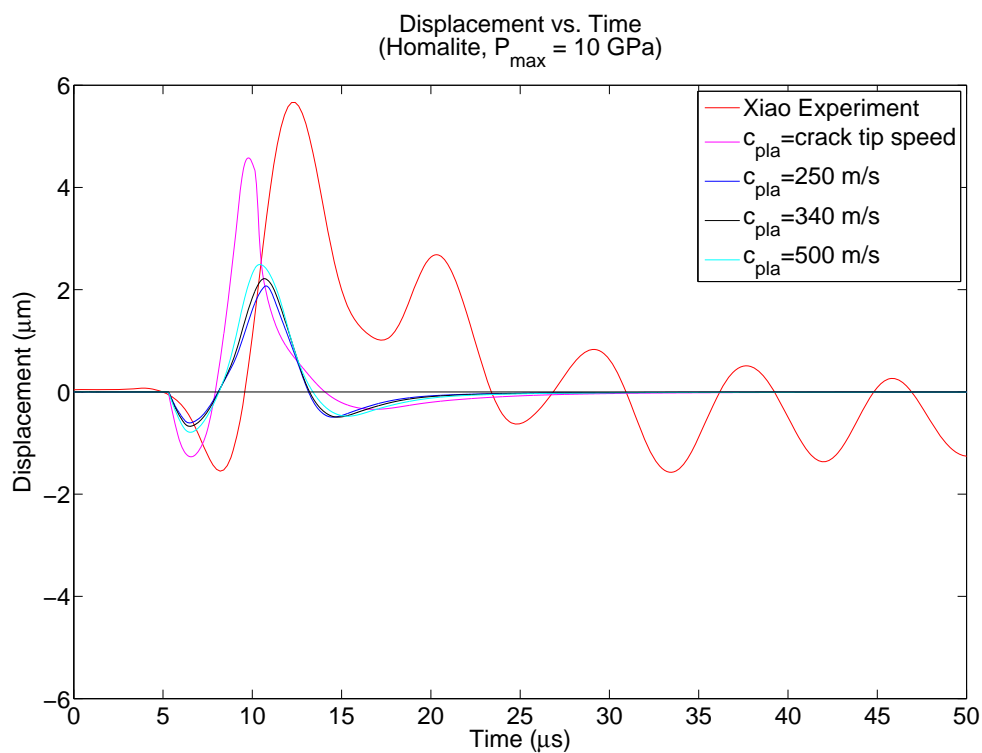


Figure 4.11: Comparison of interface-parallel displacement, for numerical simulations governed by Ortiz-Camacho cohesive zone model, at a distance of 10 mm from the point of explosion for loading profile plasma speeds of $C_{\text{pla}} = 250$ m/s, 340 m/s, 500 m/s. The loading parameters are $P_{\max} = 10$ GPa, $t_1 = 1 \mu$, $t_2 = 4 \mu\text{s}$, $t_3 = 5 \mu\text{s}$

4.2 Mode I crack propagation due to the nucleation procedure

In this section we study mode I crack caused by the explosive nucleation. We use the loading profile with parameters $P_{\max} = 10 \text{ GPa}$, $t_1 = 1 \mu\text{s}$, $t_2 = 4 \mu\text{s}$ and $t_3 = 5 \mu\text{s}$. we consider the growth of mode I crack in the region of -1 mm to +1 mm around the point of explosion. The snapshots of opening velocity are shown in Figures 4.12 - 4.14 and the snapshots of opening displacements are shown in Figures 4.15 - 4.17.

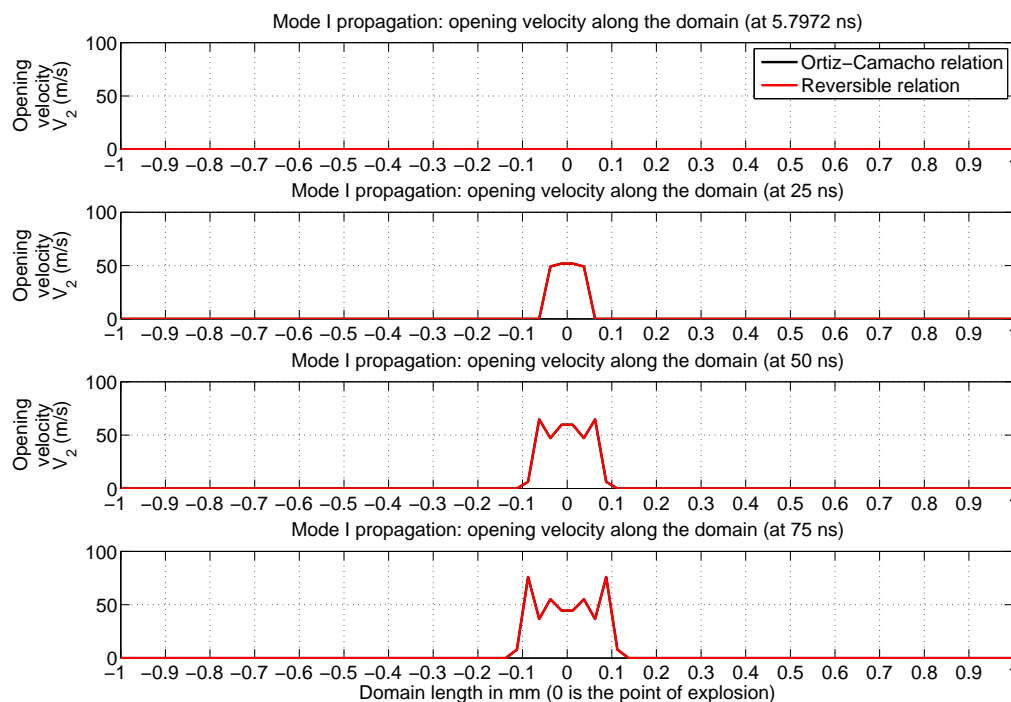


Figure 4.12: Opening velocity in the nucleation region (at $t = 0, 25, 50, 75 \text{ ns}$)

The further growth of crack on the scale of -10 mm to +10 mm from the point of explosion, is shown in Figures 4.18 - 4.23.

We find that the opening mode propagates several mm away from the point of explosion on either side. Figure 4.22 shows that at $t = 7 \mu\text{s}$, when most of the interface closes, the mode I crack has propagated about 14 mm. This region is comparable

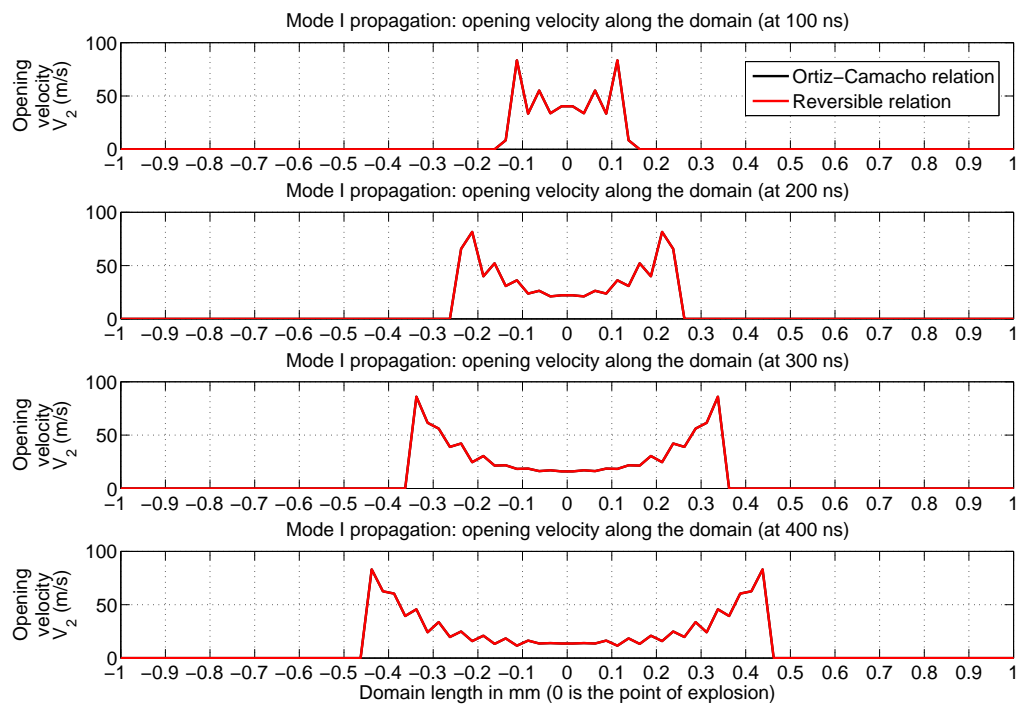


Figure 4.13: Opening velocity in the nucleation region (at $t = 0.1, 0.2, 0.3, 0.4 \mu\text{s}$)

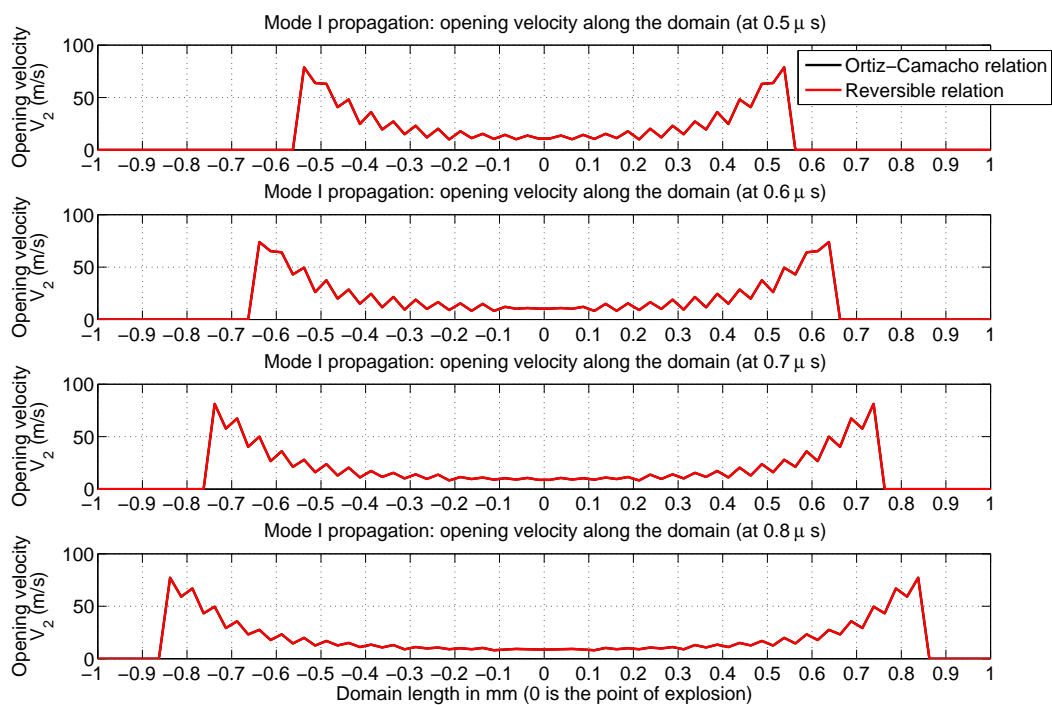


Figure 4.14: Opening velocity in the nucleation region (at $t = 0.5, 0.6, 0.7, 0.8 \mu\text{s}$)

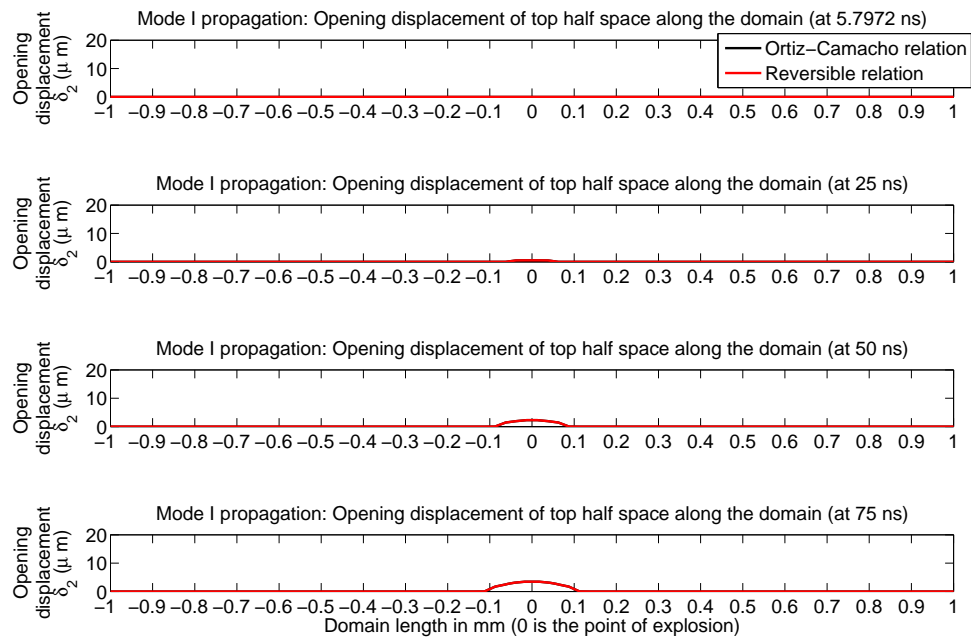


Figure 4.15: Opening displacement in the nucleation region (at $t = 0, 25, 50, 75$ ns)

to the length of the metallic particle deposition observed in the experiments. Note that in Figures 4.12-4.23, the results are plotted for two cohesive zone laws Ortiz-Camacho cohesive zone law and reversible rate-independent cohesive zone law. As expected from the results described in the earlier sections, the simulations with both laws give nearly identical results. Only in Figures 4.19 and 4.20 the closing velocities as governed by the two cohesive zone models differ as theoretically expected.

4.3 Conclusions

Thus, in this chapter we have modeled the effects of the nucleation mechanism in the dynamic rupture experiments and determined parameters that would simulate the explosion conditions. The parameters were determined by comparing the interface-parallel displacements from the numerical simulations with the experimental results of Lu (2009). We have numerically observed the existence of mode I crack due to the nucleation conditions. From the parameter study we conclude that:

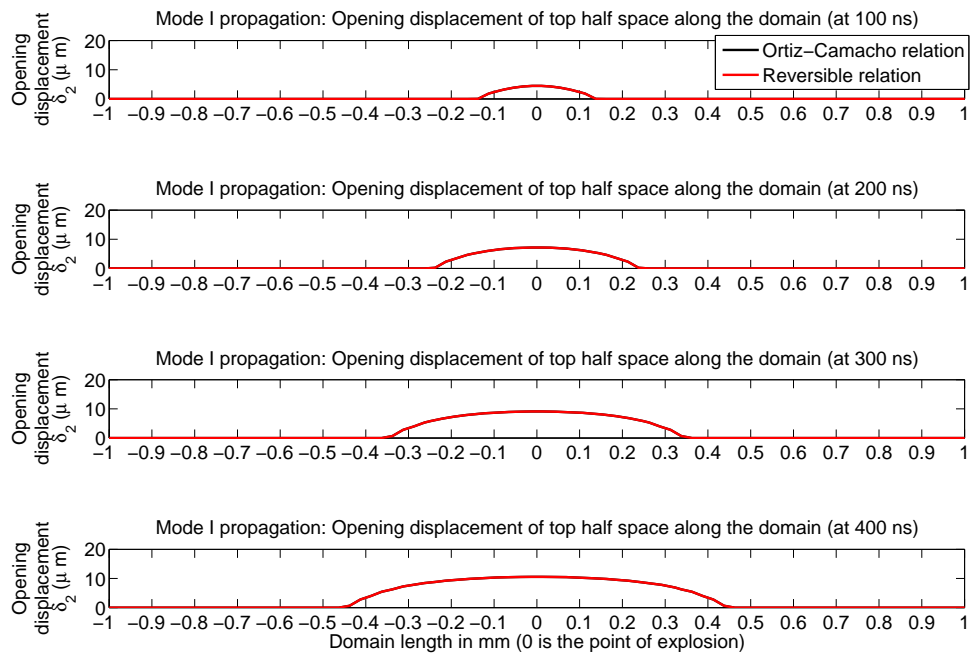


Figure 4.16: Opening displacement in the nucleation region (at $t = 0.1, 0.2, 0.3, 0.4 \mu\text{s}$)

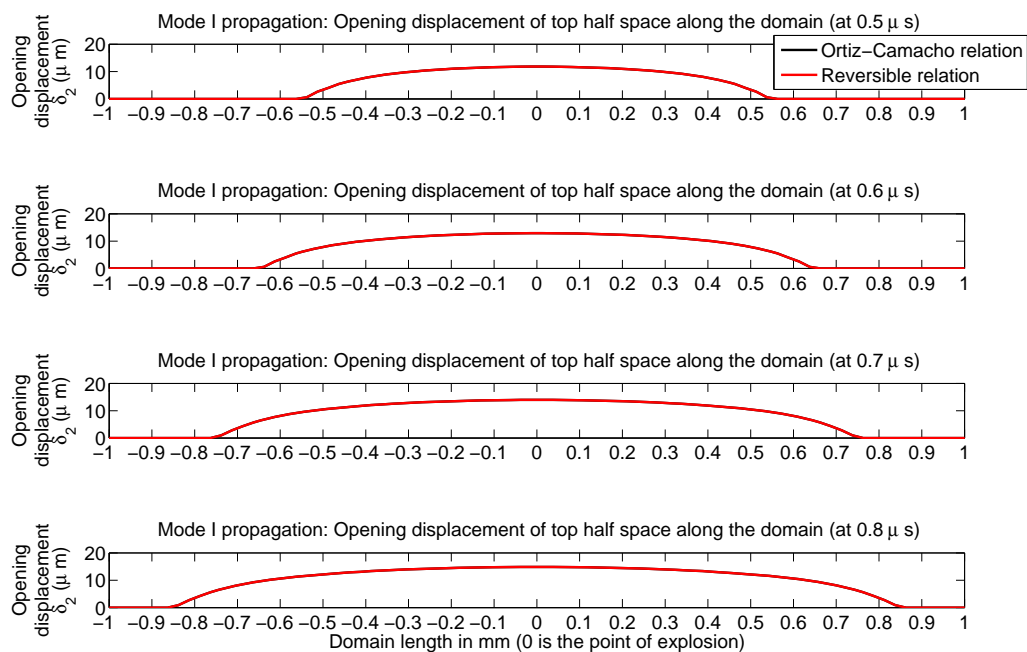


Figure 4.17: Opening displacement in the nucleation region (at $t = 0.5, 0.6, 0.7, 0.8 \mu\text{s}$)

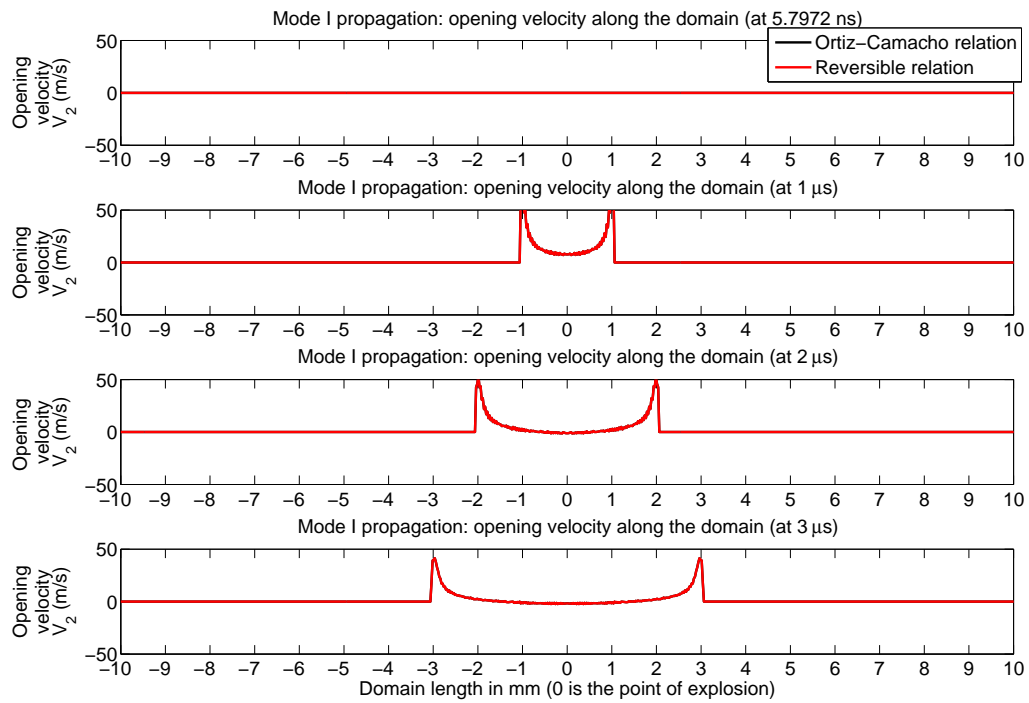


Figure 4.18: Opening velocity in the domain (at $t = 1, 2, 3, 4 \mu$ s)

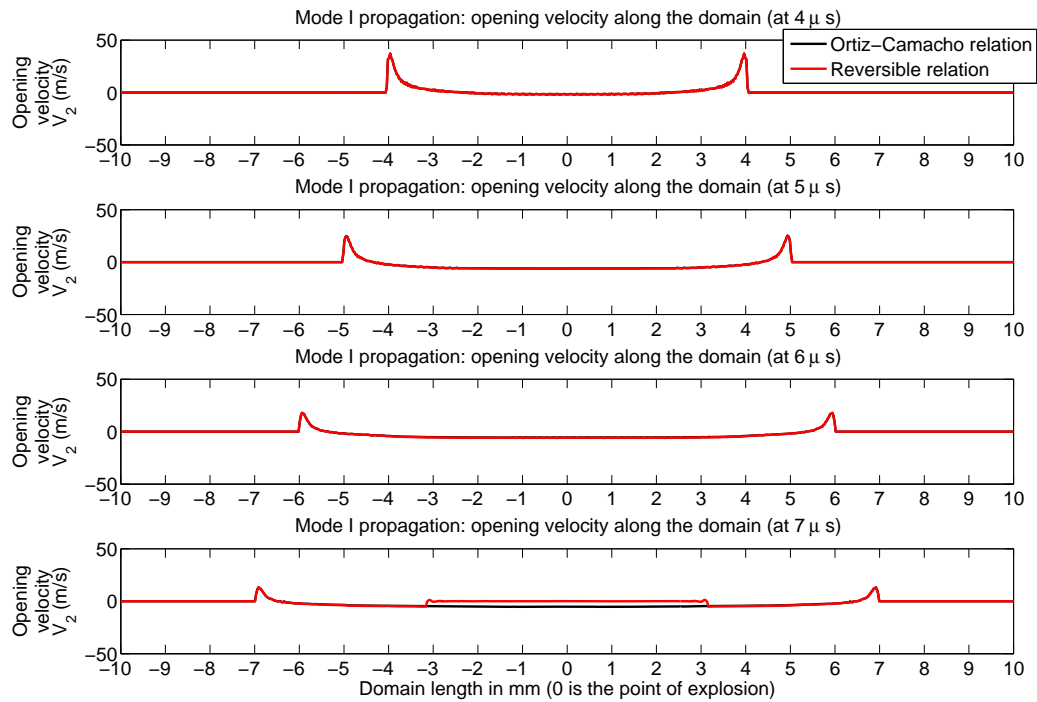


Figure 4.19: Opening velocity in the domain (at $t = 5, 6, 7, 8 \mu$ s)

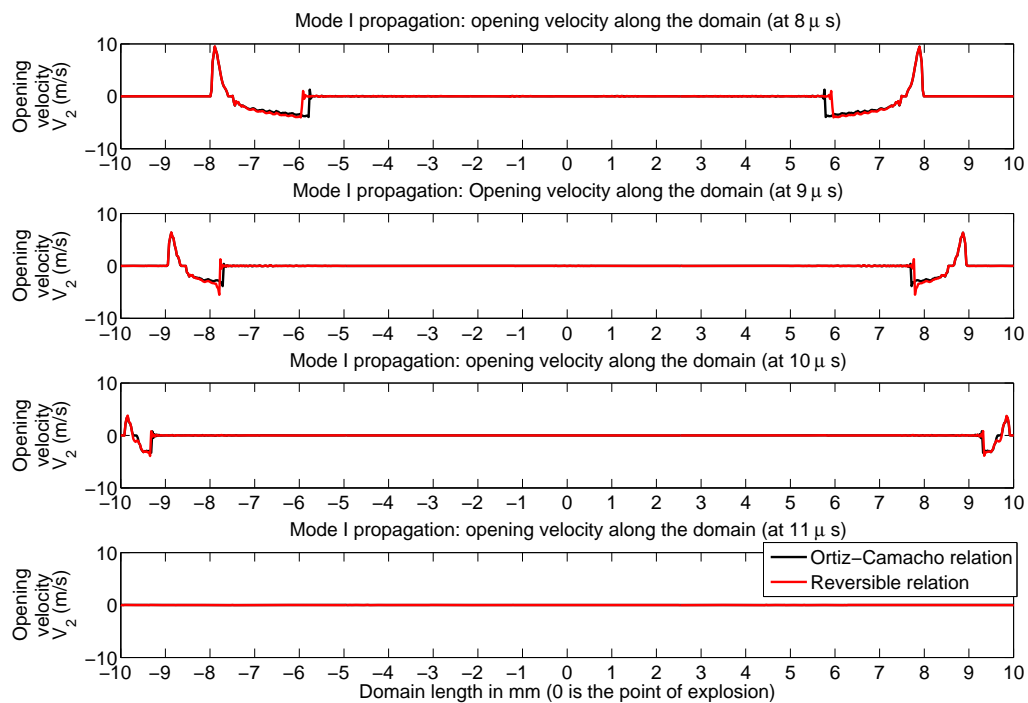


Figure 4.20: Opening velocity in the domain (at $t = 9, 10, 11, 12 \mu$ s)

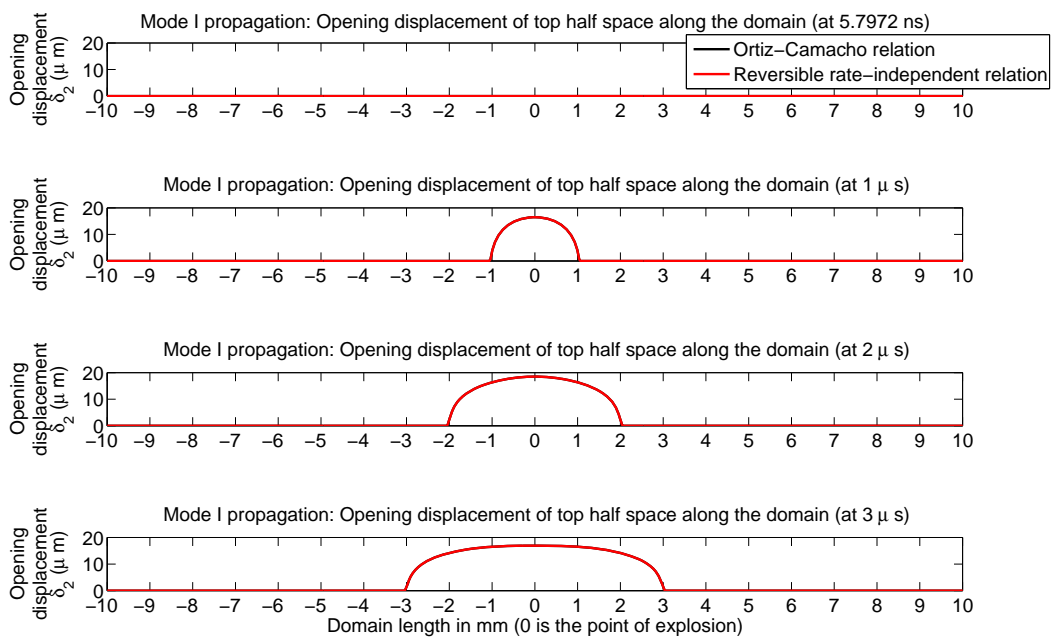


Figure 4.21: Opening displacement in the domain (at $t = 1, 2, 3, 4 \mu$ s)

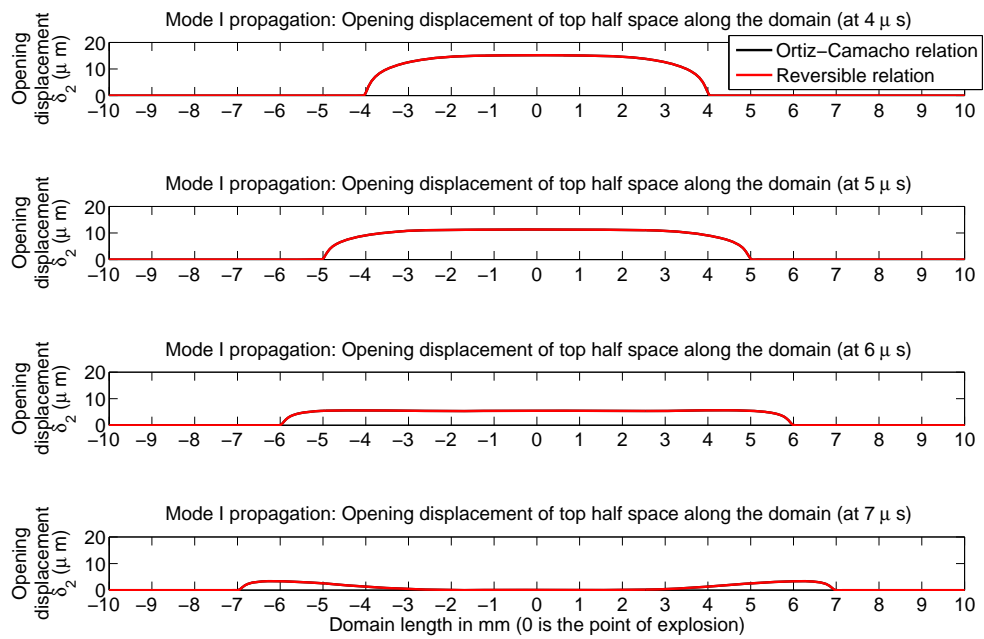


Figure 4.22: Opening displacement in the domain (at $t = 5, 6, 7, 8 \mu\text{s}$)

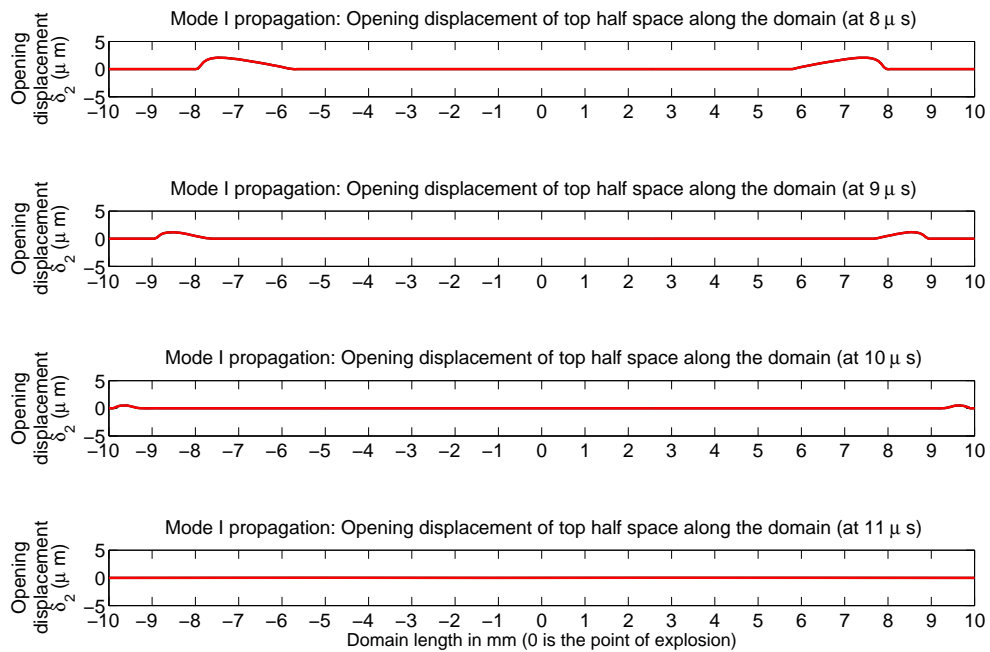


Figure 4.23: Opening displacement in the domain (at $t = 9, 10, 11, 12 \mu\text{s}$)

1. The loading profile considered matches the experimentally measured particle velocities reasonably well, given the anticipated discrepancies between 2D modeling used and the 3D nature of the experiments.
2. The maximum pressure due to the wire explosion is of the order of 10 GPa.
3. For the loading profiles considered, and the plasma spreading speeds that are equal to the crack tip speed the time parameters that best simulate the explosion process are $t_1 = 2\mu s$, $t_1 = 6\mu s$ and $t_1 = 7\mu s$.
4. The plasma spreading speed has a significant effect on the interface-parallel velocities and needs further investigation.
5. The cohesive zone models considered have negligible effect on the opening displacements and velocities due to the fact that there is no reopening of the interface.
6. The extent of the mode I crack created by the explosion is comparable to the length of the metallic particle deposition observed in the experiments.

4.4 Future work

The loading profiles considered resulted in narrower pulse of interface-parallel motion than the explosion process in the dynamic rupture experiments. So future work is needed to investigate more loading profiles.

Another direction for future work involves understanding the process of explosion from the point of view of plasma physics and to build more accurate models that can predict the flow of plasma as the crack propagates.

The finite thickness of the plate used in the dynamic rupture experiments creates three dimensional effects close to the nucleation region. Future work is needed to

study the three-dimensional effects using the Spectral Element Method developed by Kaneko *et al.* (2008).

References

- AAGAARD, B.T., HEATON, T.H. & HALL, J.F. (2001). Dynamic earthquake ruptures in the presence of lithostatic normal stresses: Implications for friction models and heat production. *Bull. Seism. Soc. Amer.*, **91**, 1765–1796.
- ABRAHAM, F.F. & GAO, H. (2000). How fast can cracks propagate? *Phys. Rev. Lett.*, **84**, 3113–3116.
- ANDREWS, D.J. (1976). Rupture velocity of plane strain shear cracks. *J. Geophys. Res.*, **81**, 5679–5687.
- ANDREWS, D.J. (1985). Dynamic plane-strain shear rupture with a slip weakening friction law calculated by a boundary integral method. *Bull. Seism. Soc. Amer.*, **75**, 1–21.
- ANDREWS, D.J. & BEN-ZION, Y. (1997). Wrinkle-like slip pulse on a fault between different materials. *J. Geophys. Res.*, **102**, 553–571.
- AOCHI, FUKUYAMA, H.E. & MATSU'URA, M. (2000). Selectivity of spontaneous rupture propagation on a branched fault. *Geophys. Res. Lett.*, **27**, 3635–3638.
- BARENBLATT, G.I. (1959). Concerning equilibrium cracks forming during brittle fracture: The stability of isolated cracks, relationships with energetic theories. *Appl. Math. Mech.*, **23**, 1273–1282.
- BEN-ZION, Y. & RICE, J.R. (1997). Dynamic simulations of slip on a smooth fault in an elastic solid. *J. Geophys. Res.*, **102**, 17771–17784.

- BREITENFELD, M.S. & GEUBELLE, P.H. (1998). Numerical analysis of dynamic debonding under 2d in-plane and 3d loading. *Int. J. Fracture*, **93**, 13–38.
- BROBERG, K.B. (1989). The near-tip field at high crack velocities. *Int. J. Fracture*, **39**, 1–13.
- BURRIDGE, R. (1973). Admissible speeds for plane-strain self-similar shear cracks with friction but lacking cohesion. *Geophys. J. Royal Astro. Soc.*, **35**, 439–455.
- BURRIDGE, R., CONN, G. & FREUND, L.B. (1979). Stability of a rapid mode-ii shear crack with finite cohesive traction. *J. Geophys. Res.*, **84**, 2210–2222.
- CAMACHO, G.T. & ORTIZ, M. (1996). Computational modeling of impact damage in brittle materials. *Int. J. Solids Struct.*, **33**, 2899–2938.
- COCHARD, A. & MADARIAGA, R. (1994). Dynamic faulting under rate-dependent friction. *Pure Appl. Geophys.*, **142**, 419–445.
- COCHARD, A. & RICE, J.R. (2000). Fault rupture between dissimilar materials: Ill-posedness, regularization and slip-pulse response. *J. Geophys. Res.*, **105**, 25891–25907.
- DAS, S. (1980). A numerical method for determination of source time functions for general three-dimensional rupture propagation. *Geophys. J. R. Astr. Soc.*, **62**, 591–604.
- DAS, S. & AKI, K. (1977). Numerical study of 2-dimensional spontaneous rupture propagation. *Geophys. J. Royal Astro. Soc.*, **50**, 643–668.
- DAS, S. & KOSTROV, B.V. (1988). An investigation of the complexity of the earthquake source time function using dynamic faulting models. *J. Geophys. Res.*, **93**, 8035–8050.
- DAY, S.M. (1982). Three-dimensional simulation of spontaneous rupture - the effect of non-uniform prestress. *Bull. Seismol. Soc. Am.*, **72**, 1881–1902.

- DAY, S.M., DALGUER, L.A., LAPUSTA, N. & LIU, Y. (2005). Comparison of finite difference and boundary integral solutions to three-dimensional spontaneous rupture. *J. Geophys. Res.*, **110**, B12307.
- DIX, C.H. (1954). The method of cagniard in seismic pulse problems. *Geophysics*, **19**, 722–738.
- DUGDALE, D.S. (1960). Yielding of steel sheets containing slits. *J. Mech. Phys. Solids*, **8**, 100–104.
- DUNHAM, E.M. & ARCHULETA, R.J. (2005). Near-source ground motion from steady state dynamic rupture plates. *Geophys. Res. Lett.*, **32**, L03302.
- FESTA, G. & VILOTTE, J.P. (2006). Influence of rupture initiation on the intersonic transition: crack-like versus pulse-like modes. *Geophys. Res. Lett.*, **33**, L15320.
- FREUND, L.B. (1979). Mechanics of dynamic shear crack propagation. *J. Geophys. Res.*, **84**, 2199–2209.
- GAO, H., HUANG, Y. & ABRAHAM, F.F. (2001). Continuum and atomistic studies of intersonic crack propagation. *J. Mech. Phys. Solids*, **49**, 2113–2132.
- GEUBELLE, P.H. & BREITENFELD, M.S. (1997). Numerical analysis of dynamic debonding under anti-plane shear loading. *Int. J. Fracture*, **85**, 265–282.
- GEUBELLE, P.H. & KUBAIR, D.V. (2001). Inter-sonic crack propagation in homogeneous media under shear-dominated loading. *J. Mech. Phys. Solids*, **49**, 571–587.
- GEUBELLE, P.H. & RICE, J.R. (1995). A spectral method for three-dimensional elastodynamic fracture problems. *J. Mech. Phys. Solids*, **43**, 1791–1824.
- GRIFFITH, A.A. (1920). The phenomena of rupture and flow in solids. *Phil. Trans. Series A*, **221**, 163–198.
- INGLIS, C.E. (1913). Stresses in a plate due to the presence of cracks and sharp corners. *Trans. Inst. Naval Arch.*, **55**, 219–241.

- KAME, N. & YAMASHITA, T. (1999). Simulation of spontaneous growth of crack without constraints on the crack tip path. *J. Geophys. Res.*, **139**, 345–358.
- KANEKO, Y., LAPUSTA, N. & AMPUERO, J.P. (2008). Spectral-element modeling of spontaneous earthquake rupture on rate and state faults: Effect of velocity-strengthening friction at shallow depths. *J. Geophys. Res.*, **113**, B09317.
- LAMB, H. (1904). On the propagation of tremors over the surface of an elastic solid. *Phil. Trans. Roy. Soc.*, **203**, 1–42.
- LAPUSTA, N. & RICE, J.R. (2000). Nucleation and early seismic propagation of small and large events in a crustal earthquake model. *Geophys. Res. Lett.*, **27**, 3635–3638.
- LAPUSTA, N., RICE, J.R., BEN-ZION, Y. & ZHANG, G. (2000). Elastodynamic analysis for slow tectonic loading with spontaneous rupture episodes on faults with rate- and state-dependent friction. *J. Geophys. Res.*, **105**, 23765–23789.
- LIU, Y. (2009). *Three-dimensional elastodynamic modeling of frictional sliding with application to intersonic transition..* Ph.D. thesis, California Institute of Technology.
- LIU, Y. & LAPUSTA, N. (2008). Transition of mode II cracks from sub-Rayleigh to intersonic speed in the presence of favorable heterogeneity. *J. Mech. Phys. Solids*, **56**, 25–50.
- LU, X. (2009). *Combined experimental and numerical study of spontaneous dynamic rupture on frictional interfaces..* Ph.D. thesis, California Institute of Technology.
- LU, X., LAPUSTA, N. & ROSAKIS, A.J. (2007). Pulse-like and crack-like ruptures in experiments mimicking crustal earthquakes. *Proc. Natl. Acad. Sci. USA*, **104**, 18931–18936.

- LU, X., LAPUSTA, N. & ROSAKIS, A.J. (2009). Analysis of supershear transition regimes in rupture experiments: the effect of nucleation conditions and friction parameters. *Geophys. J. Int.*, **177**, 717–732.
- MADARIAGA, R. & OLSEN, K.B. (2000). Criticality of rupture dynamics in 3-d. *Pure Appl. Geophys.*, **157**, 1981–2001.
- MUSKHELISHVILI, N.I. (1975). *Some basic problems of mathematical theory of elasticity*. Springer.
- NEEDLEMAN, A. & ROSAKIS, A.J. (1999). The effect of bond strength and loading rate on the conditions governing the attainment of intersonic crack growth along interfaces. *J. Mech. Phys. Solids*, **47**, 2411–2449.
- ORTIZ, M. & PANDOLFI, A. (1999). Finite-deformation irreversible cohesive elements for three-dimensional crack-propagation analysis. *Int. J. Numerical Methods in Engineering*, **44**, 1267–1282.
- PEKERIS, C.L. (1955). The seismic surface pulse. *Proc. Nat. Acad. Sciences U.S.A.*, **41**, 469–480.
- PERRIN, G., RICE, J.R. & ZHENG, G. (1995). Self-healing slip pulse on a frictional surface. *J. Mech. Phys. Solids*, **43**, 1461–1495.
- RICE, J.R. (1980). The mechanics of earthquake rupture. *Physics of Earth's Interior*, 555–649.
- ROSAKIS, A.J., XIA, K.W., LYKOTRAFITIS, G. & KANAMORI, H. (2007). Dynamic shear rupture in frictional interfaces: Speeds, directionality and modes. *in Treatise in Geophysics*.
- SHI, Z., BEN-ZION, Y. & NEEDLEMAN, A. (2008). Properties of dynamic rupture and energy partition in a solid with a frictional interface. *J. Mech. Phys. Solids*, **56**, 5–24.

- TEMPLETON, E.L., BAUDET, A., BHAT, H.S., DMOWSKA, R., RICE, J.R., ROSAKIS, A.J., & ROUSSEAU, C.E. (????). Finite element simulations of dynamic shear rupture experiments and dynamic path selection along kinked and branched faults (in press). *J. Geophys. Res.*
- XIA, K. (2005). *Laboratory investigations of earthquake dynamics.* Ph.D. thesis, California Institute of Technology.
- XIA, K.W., ROSAKIS, A.J. & KANAMORI, H. (2004). Laboratory earthquakes: The sub-rayleigh-to-supershear rupture transition. *Science*, **303**, 1859–1861.
- XU, X.P. & NEEDLEMAN, A. (1994). Numerical simulations of fast crack growth in brittle solids. *J. Mech. Phys. Solids*, **42**, 1397–1434.
- YU, C., PANDOLFI, A., ORTIZ, M., COKER, D. & ROSAKIS, A.J. (2002). Three-dimensional modeling of intersonic shear-crack growth in asymmetrically loaded unidirectional composite plates. *Int. J. Solids and Structures*, **39**, 6135–6157.